

Simulation and Measurement-Based Characterization of the Transmitting, Receiving and Scattering Figures of UAV Wireless Station

M. U. B. Awan (Author)
Radio Systems Group
University of Twente
Enschede, Netherlands
m.u.b.awan@student.utwente.nl

Dr. A. Kokkeler (Committee Chair)
 Dr. Y. Miao (Daily Supervisor)
 Dr. A. A. Glazunov (Examiner)
 Dr. L. V. Duc (External Examiner)
University of Twente

Dr. A. Mersha (Acknowledged Person)
University of Saxion

I. INTRODUCTION

The development of Unmanned Aerial Vehicles (UAV) has enabled diverse engineering applications during the last decade. UAVs have been used for surveillance and security purposes as well as for search and rescue operations in areas hit by natural disasters.

A UAV Wireless Station consists of a transceiver antenna system attached to the flying UAV platform which provides services to the users (access network) using the backhaul network [1]. The services may be cellular call and internet services in support to the existing cellular network infrastructure or to deploy on demand. The number of UAVs required for the application network varies from one UAV for on demand application to many UAVs to support the whole cellular network infrastructure. UAV wireless station has a great potential in providing line of sight wireless connectivity/services to the ground users as well as to the aerial nodes (secondary UAV wireless stations) with flexibility and low cost [2,3].

The UAV wireless station assisted network consists of stakeholders/users and infrastructure as shown in Fig. 1. Existing cellular infrastructure has mobile users connected to fixed base stations which are further connected to the core network. The advantage of using UAV wireless station along with existing infrastructure is to pick up the slack in the event of a fixed base station malfunctioning or any overloading. UAV wireless station can also extend services to the users where infrastructure is not present due to its facile deployability [4].

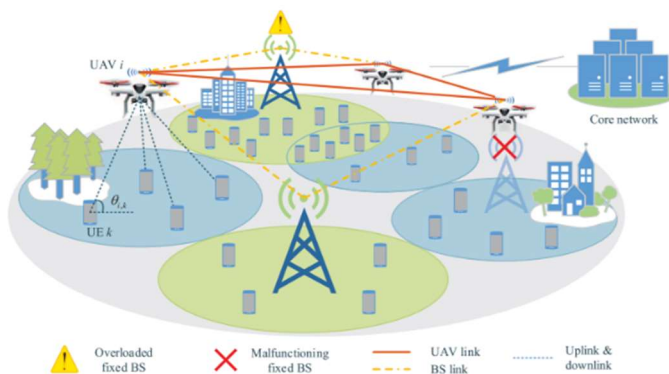


Fig. 1. Wireless station assisted network [4]

The design parameters of a wireless system, including the carrier frequency, transmitting power, antenna type and placement, define its transmission capabilities. The main ingredients of UAV wireless station are its radiating elements

which transmit or receive propagating waves, and communicate with different infrastructure at different heights, namely, users on the ground, fixed base stations (relatively higher than ground level users) and other UAV wireless stations typically at the same height as itself.

The UAV wireless station performs under conditions of radio propagation channel. Depends on the antenna type and placement (location and orientation) on UAV as well as UAV type (small deployable rotary drone), the radiated waves may experience the near field scattering (single or multiple bouncing) from its own propellers as well as the scattering from propellers of destination aerial nodes.

The transmitting, receiving, and scattering (TRS) figures of UAV wireless station shall be studied as an ensemble whole to take the **antenna placement, UAV body frame, and propeller rotation** influences into account. Fig. 2. depicts the potential influence of UAV propellers, including the scattering and backscattering from rotating blades, on the links of UAV wireless station communicating with secondary aerial nodes and ground users.

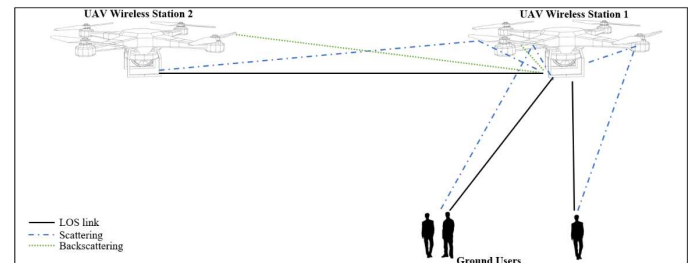


Fig. 2. UAV wireless station: TRS figures and links

On the one hand, to characterize the influence of antenna placement and UAV body frame on TRS figures, the coverage of the UAV wireless station is one key indicator no matter for Air-to-Air (A2A) or Air-to-Ground (A2G) communication scenarios. On the other hand, to characterize the influence of the propeller's rotation on the TRS figures, the micro-Doppler effect, resulted from the electromagnetic (EM) waves interacting with rotating blades and mechanical vibrations, is one key indicator, where sidebands are introduced in Doppler-frequency spectrum [5].

In this paper, the influences of 1) the antenna placement in context of UAV body frame and 2) the propeller rotation on the key indicators (metrics) characterizing the TRS figures of UAV wireless station are investigated using both simulation and measurement approaches.

This paper is organized as follows. In Section II, the literature review is performed and the motivation for conducting this research is illustrated. In Section III, the study

of antenna placement and TRS figure is performed and simulation results are shown. In Section IV, the study on rotating propeller and TRS figure is performed and simulation results are shown. Section V shows the SDR-based measurement campaign and analysis on micro-doppler effect. Section VI concludes this paper.

II. LITERATURE REVIEW AND MOTIVATION

Most of the research in literature focused on the coverage of UAV wireless station for A2G applications. The ground coverage is enabled with different antenna designs, including planar super J-pole antennas [6], circularly polarized (CP) antenna with four coupling arcs [7], cylindrical DRA [8] and conformal antenna [9] without considering the influence of UAV body frame and antenna placement. A2G measurements (throughput and received power) have also been conducted [10,11] using dipole antennas placed in two different orientations (vertical and horizontal) and monopole antenna array placed on fixed wing UAV (Telemaster). The impact of UAV body on the A2G coverage for log-periodic antenna in single orientation have been discussed in [12]. The electromagnetic interferences between multiple antennas have been simulated and investigated for antenna placements in different complex scenarios such as automated warehouse environment, helicopter and automobiles [13-15].

The scattering properties of the UAV propeller are defined by its Radar Cross Section (RCS). The RCS measurements of a UAV by using a VNA and horn antenna in an anechoic chamber has been discussed in [16]. Scattering from rotating propellers having multiple blades and sizes are also very well documented in [17,18]. In [19-21], the mathematical modelling regarding scattering from a small rotary UAV's propeller is discussed. The backscattering from UAV wireless station rotating propellers directly influences its TRS figures in A2A applications. For this purpose, micro-Doppler signature can be observed due to the backscattering from rotational motion of propellers. Analysis of the micro-Doppler effect, its theory and measurement details regarding UAV propeller are well documented in [22-24]. In [25], changes in the RCS measurements in near field region have been discussed. Helicopter Rotation Modulation (HERM) lines analysis is also required to study the side bands produced due to micro-Doppler effect. The HERM lines measurement details are also available in literature [26].

The focus of most of the aforementioned research is towards A2G coverage and its link performance using few antenna placement scenarios on a fixed wing drone. A uniform simulation- and measurement-based study on antenna placement for optimizing A2A coverage for rotatory drones considering the influence of rotation mobility is missing. The major source of scattering around UAV wireless station are propellers in rotational mobility. Therefore, it is important to study the influence of antenna placement on UAV body frame and propeller rotation in order to guarantee the robustness for integrated A2G-A2A functionality of UAV wireless station.

To this end, the objective of the thesis is to characterize the TRS figures of the UAV wireless station under the influence of propeller rotation and antenna placement on body frame. This research investigates the influences collectively for A2G and A2A scenarios. For this purpose, single antenna/multi-antenna are placed in different configurations to study the impact of UAV body frame on resultant coverage

of UAV wireless station. The distributed multi-antenna system (DMS) on UAV body frame is explored in order to get complete 3D UAV wireless station coverage for A2A and A2G scenarios. The influence of scattering from rotating propeller is also investigated on the TRS figures using the series of quasi-static rotating propeller simulations and the Software-Defined Radio (SDR) measurements. The quasi-static rotating-propeller simulations help to model the variations of propeller RCS when different source conditions illuminate the rotating propeller. The SDR measurement campaign shows the influence of backscattering from propeller by estimating the power of induced sidebands and their spread in frequency domain for different A2A settings.

III. INFLUENCE OF ANTENNA PLACEMENT AND UAV BODY FRAME ON UAV WIRELESS STATION TRS FIGURES

A. Key Metrics Characterizing TRS Figures Subject to Influence of Antenna Placement and UAV Body Frame

Here the antenna placement study is conducted for UAV wireless station to discuss the impact of antenna placement and UAV body on the TRS figures in A2A and A2G scenarios. The *coverage* is the key indicating metrics. In A2G applications, the key indicator is the coverage for ground users in the southern hemisphere of UAV wireless station. Similarly, the key indicator in A2A scenario, is the coverage of elevation angles spreading beyond equator towards northern or southern hemisphere. The coverage requirement for UAV wireless station in A2G and A2A scenarios is shown in Fig. 3, where ' θ_{A2G} ' and ' θ_{A2A} ' defines the angular spread of coverage in A2G and A2A scenarios, respectively. The A2G coverage angular spread ' θ_{A2G} ' depends on the height of UAV wireless station ' h ' and distance of ground user (standing on the coverage boundary) from the centre of the coverage. On the other hand, the A2A coverage angular spread ' θ_{A2A} ' depends on its distance ' d ' from other UAV wireless stations and difference of height ' h_A ' between them.

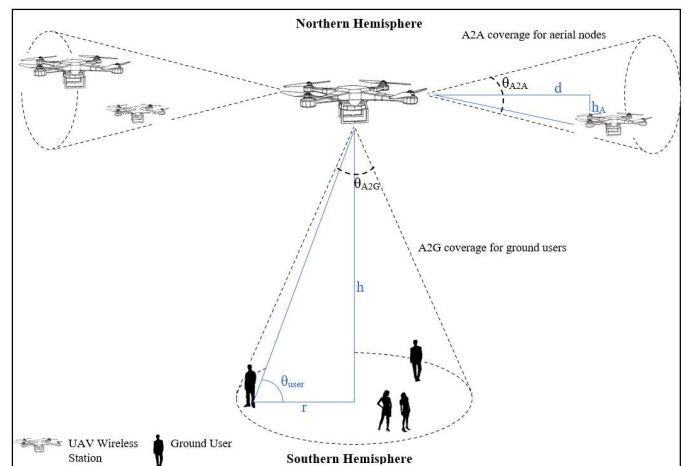


Fig. 3. UAV wireless station coverage requirements for A2G-A2A functionality

The metrics evaluating the coverage of UAV wireless station can be the *link budget* in free space. The received power of ground node in A2G scenario or the other aerial node in A2A scenario is described by using the Friis equation in dB scale given by:

$$P_r = P_t + G_t(\theta, \varphi') + G_r(\theta, \varphi') - L - L_{fs} \quad (1)$$

where ‘ P_r ’ and ‘ P_t ’ are received and transmitted power, respectively. The ‘ $G_t(\theta, \varphi)$ ’ and ‘ $G_r(\theta, \varphi)$ ’ are transmitter and receiver gain where ‘ θ ’ is the elevation angle and ‘ φ ’ is the azimuth angle, respectively. The total system loss ‘ L ’ consists of antenna feeder, connector losses and other losses. The ‘ L_{fs} ’ is the free space path loss defined by the distance ‘ d ’ between link ends and the operating frequency ‘ f ’.

The workflow of the influence of antenna placement and UAV body frame on the UAV wireless station TRS figures is shown in Fig. 4. The first step is to compute the complex-valued radiation pattern of integrated antenna/antennas and UAV body frame for different antenna placement scenarios. It gives the gain distribution over the UAV wireless station. The coverage (key indicator for TRS figures) is the UAV wireless station reachability to the ground users and aerial nodes, therefore, link budgeting is required to ensure the quality of link by comparing scenarios using gain threshold in desired directions.

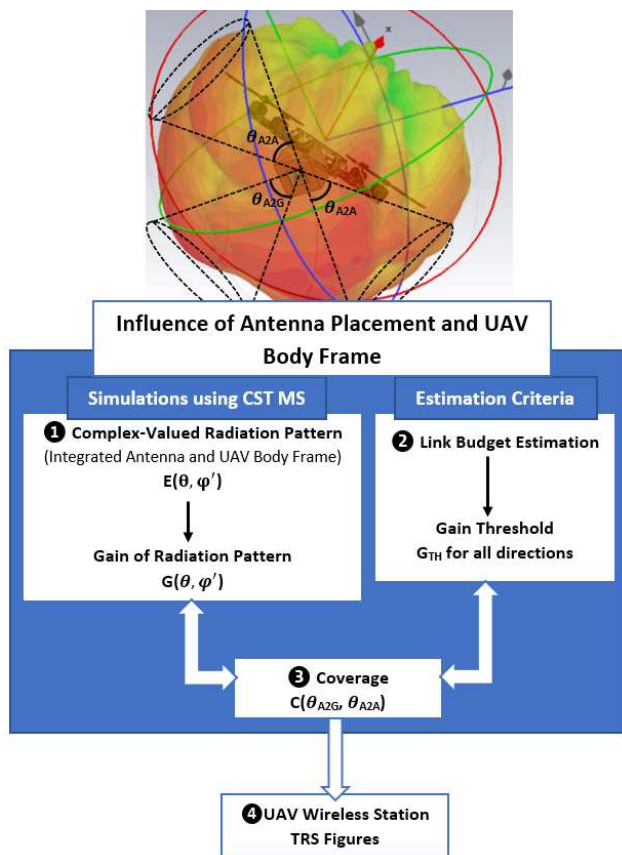


Fig. 4. Influence of antenna placement and UAV body frame on TRS figures work flow

B. Simulation of Radiation Pattern of Integrated Antenna Placed on UAV Body Frame

UAV body frame may act as a reflector due to the lossy nature of material. The standalone antenna radiation pattern changes after integrating with UAV main body frame. Where to place the antennas on UAV and what is the radiation pattern of the integrated antennas and UAV body determine the TRS figure, hence, the functionality of the UAV wireless station.

The geometry of body frame of UAV varies with the type of aircraft, for instance rotary wing aircrafts have extended arms while fixed wing aircrafts have extended wings, as shown in Fig. 5. Mainly, aluminium, steel or carbon-fiber

reinforced plastic materials are used to build the body frame [27]. The purpose of using carbon-fiber or light metal alloy materials in UAVs is to provide strength while keeping it as light weight as possible. Both materials have lossy conductor properties.



Fig. 5. UAV body frames (metallic, carbon fiber reinforced plastic and aluminium)

Throughout this section, a small sized quadcopter UAV model was selected for antenna placement simulations with dimension of 1000 mm x 1180 mm x 500 mm. It is a good candidate for UAV wireless station due to its stable flight and hovering capabilities. Antenna placement on a small sized UAV is tricky because of its design. The quadcopter has four extended arms for placement of rotors and therefore, only limited area of body frame left for antenna placement. The placement of antenna under any rotor is not practical because air drag can cause bending or damaging to the antenna. Moreover, improper antenna placement induces variations on radiation pattern hence disturbs the coverage stability.

The antenna placement investigations on UAV body frame were carried out in CST microwave studio by placing antennas at different locations and configurations considering the UAV propellers at fixed position. **The complex-valued radiation pattern of integrated antenna and UAV body frame is computed by the CST solver as the indicating TRS figure.** From the TRS figure, the coverage of UAV wireless station for A2A or A2G connections can be established for performance evaluation of the functionality of this wireless station.

In the simulation in CST, the detailed small UAV 3D model [28] was used during the simulation. The disadvantage of using detailed UAV 3D model is the added computational load. Therefore, the selection of efficient EM solver is required to compensate the computation time. The recommended electromagnetic solver for the CST antenna placement problem is Finite Element Method (FEM) EM solver. The FEM EM solver is efficient for modelling and dealing in detailed geometric problems because of high geometric flexibility [29]. The selection of UAV 3D model material also affects the computational load. Therefore, the material of UAV 3D model was set to Perfect Electric Conductor (PEC) to save more computation time and also to simulate the worst case scenario for antenna placement.

The resultant radiation pattern and furthermore the coverage of UAV wireless station integrating antenna and

UAV body frame depend on following factors: number, type, position, and orientation of antenna used. The selection of antenna type for UAV wireless station is usually based on the weight, shape, and standalone radiation properties of antenna. Light weight simple geometric antennas (dipole, monopole and patch) are preferred to avoid overloading the UAV and excessive air drag during flight. Non-directional antennas (dipole and patch antennas) were designed in Antenna Magus and used for the antenna placement simulation scenarios. Antenna positioning on the UAV frame is important for fulfilling the coverage requirement on the southern hemisphere region for A2G and the equatorial region for A2A in order for UAV wireless station to accommodate more ground/aerial users. The antennas can be placed in horizontal and vertical orientations presenting orthogonality (diversity) in case of multiple antennas to avoid mutual interference.

C. Numerical Examples

The operating frequency of antennas on UAV wireless station shall have no conflict with the UAV control subsystem's frequency and be based on the availability of license. The 3.3 GHz operating frequency was used in simulations to be consistent with the measurement setup in later section (restrained by hardware) and to avoid potential interferences with ISM band i.e. 802.11 (Wifi), Bluetooth etc.

The dipole and inset fed patch antennas were used for the antenna placement investigations. The purpose of using non-directional/omni-directional antennas were to provide enhanced coverage (increases coverage angular spread). Contrarily, directional antennas were discouraged here for small-sized UAV because it adds complexity in radio system (e.g., require 3D beam scanning architecture) hence increase the load. The dipole antenna has omni-directional (donut) shaped radiation pattern with 2.27 dB gain whereas radiation pattern of patch antenna is directed towards broadside of antenna with 7.69 dB gain.

The different link budget calculations using Eq.(1). shows that by setting the minimum gain value of -5 dBi gives the received power of -98.81 dBm which is comparable to the bladeRFx40 (SDR) sensitivity -110 dBm [30]. Hence, minimum gain value calculated through link budget sets the threshold for comparing complex-valued radiation patterns for different antenna placement scenarios.

The UAV wireless station coverage is the A2A-A2G angular spread of computed complex-valued radiation pattern (integrated antenna and UAV body frame) in desired directions, above the set gain threshold. The A2G coverage angular spread ' θ_{A2G} ' has already been defined in literature for different A2G scenarios, for instance, for suburban, urban, dense urban and high-rise urban, defined as 139.32°, 95.12°, 70.76° and 28.96°, respectively [31]. There is no clear reference of coverage requirements for A2A scenario in literature. Therefore, the figure of merits for A2A-A2G scenario in Fig. 6 is based upon the assumption that height variation of UAVs is not significant. The antenna placement scenarios are compared using figure of merits defined as $\theta_{A2G} = 120^\circ$ (210° to 330°) for A2G scenario and $\theta_{A2A} = 60^\circ$ (150° to 210° and 330° to 390°) for A2A scenario.

In following examples, the 3D coverage map of UAV wireless station is inspected in two orthogonal planes. The cut planes are represented by blue and black arrows as shown in Fig. 7.

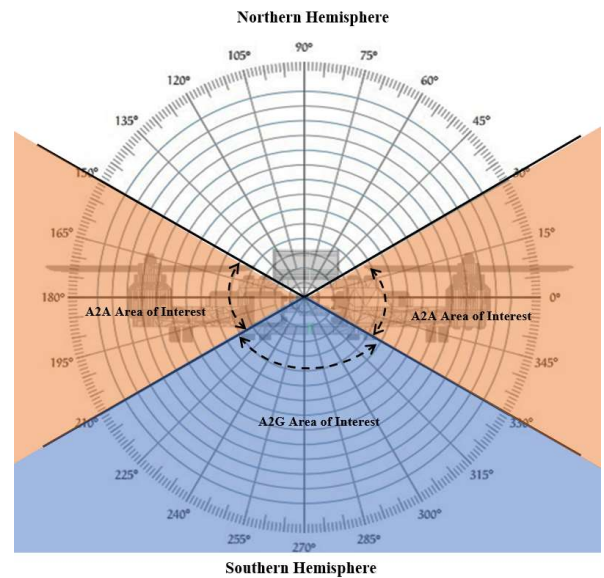


Fig. 6. Figure of merits: the angular spread of UAV wireless station coverage on polar plot, the orange is for A2A and the blue is for A2G

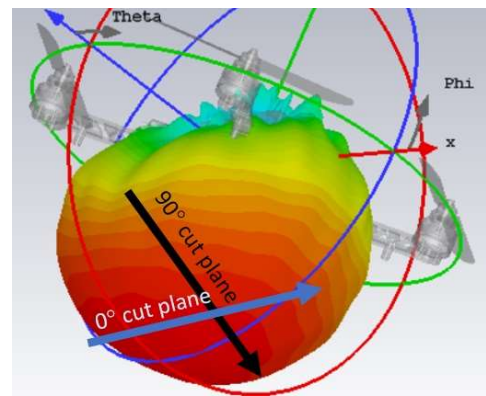


Fig. 7. Coverage cut planes at cut angles 0° and 90°

The position of UAV is represented by UAV equator lines in resultant coverage plots. The blue portion represents the A2G coverage angular spread ' θ_{A2G} ' whereas the orange portion represents the A2A coverage angular spread ' θ_{A2A} '. The portion below the -5dBi gain threshold is the no coverage area for UAV wireless station.

1) Single Antenna Placement & Coverage

The single patch and dipole antenna (horizontal and vertical orientations) were placed under the UAV body frame one by one to see its impact on the resultant UAV wireless station coverage.

The dipole antenna placement at a distance of 10mm in horizontal orientation with respect to the UAV body frame as shown in Fig. 8, and its complex-valued radiation pattern for both planes are shown in Fig. 9.

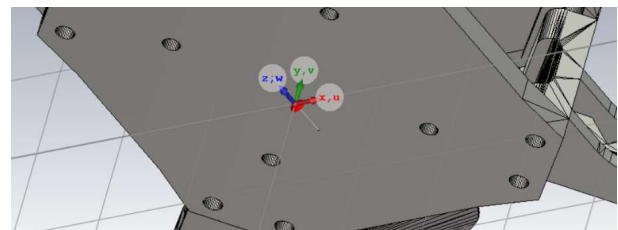


Fig. 8. Dipole antenna placement in horizontal orientation

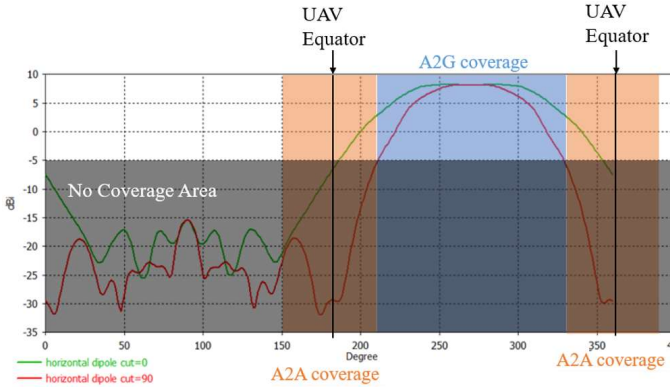


Fig. 9. Radiation pattern of integrated horizontal dipole antenna and UAV body frame for cut plane 0°(green) and 90°(red)

The second single antenna placement scenario is vertically placed dipole antenna at a distance of 10mm with respect to the UAV body frame as shown in Fig. 10, and its complex-valued radiation pattern at both planes is shown in Fig. 11.

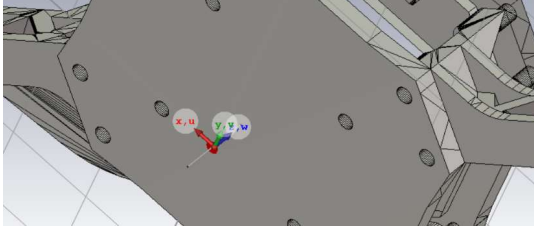


Fig. 10. Dipole antenna placement in vertical orientation

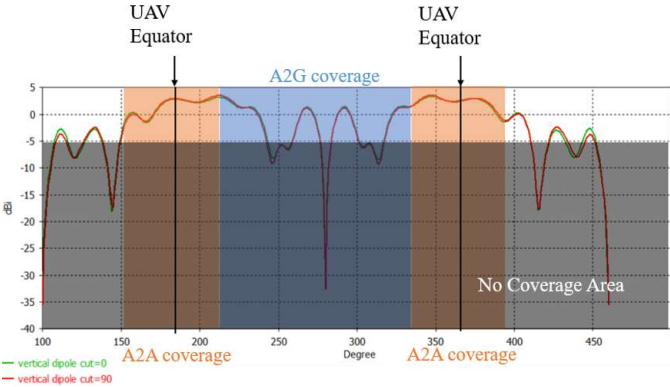


Fig. 11. Radiation pattern of integrated vertical dipole antenna and UAV body frame for cut plane 0°(green) and 90°(red)

The patch antenna was also placed on UAV body frame facing towards the southern hemisphere as shown in Fig. 12, and its coverage is shown in Fig. 13.

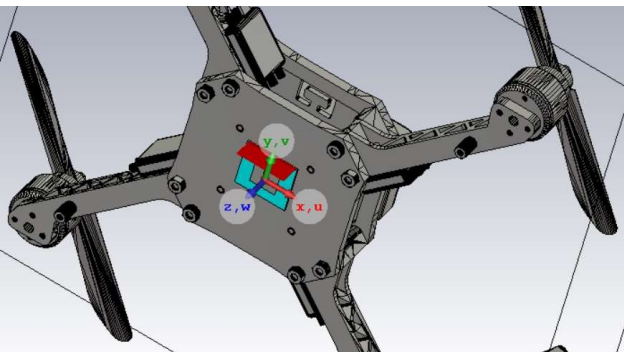


Fig. 12. Patch antenna placement

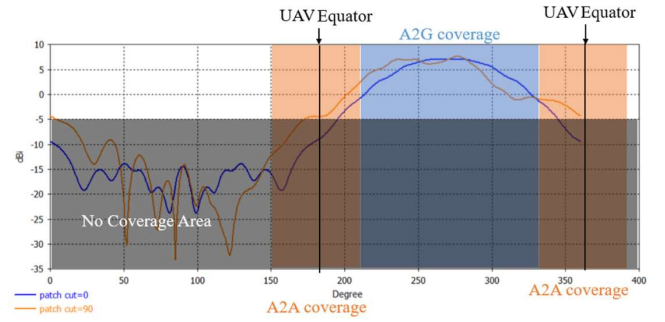


Fig. 13. Radiation pattern of integrated patch antenna and UAV body frame for cut plane 0°(blue) and 90°(orange)

The UAV wireless station coverage estimated from complex-valued radiation pattern of single antenna placement scenarios using defined figure of merits is presented and compared in TABLE I.

TABLE I: SINGLE ANTENNA PLACEMENT COVERAGE COMPARISON

Single Antenna Scenario	A2G Coverage		A2A Coverage	
	Cut Plane 0°	Cut Plane 90°	Cut Plane 0°	Cut Plane 90°
Dipole Antenna (Horizontal orientation)	210° to 330°	210° to 330°	186° to 210° and 330° to 364°	Nil
Dipole Antenna (Vertical orientation)	210° to 330° with three nulls at 250°(16° wide), 275°(5° wide) and 305°(16° wide)	210° to 330° with three nulls at 250°(16° wide), 275°(5° wide) and 305°(16° wide)	150° to 210° and 330° to 390°	150° to 210° and 330° to 390°
Patch Antenna	210° to 330°	210° to 330°	196° to 210° and 330° to 344°	172° to 210° and 330° to 360°

The comparison between single antenna placement scenarios show that patch and dipole antenna (horizontal orientation with respect to UAV body frame) are suitable for only A2G coverage but they have incomplete coverage along UAV equator which doesn't allow them to give integrated A2A-A2G coverage. The main lobe of the patch antenna radiation pattern tilted after interacting with the UAV body frame. However, the dipole antenna (vertical orientation with respect to UAV body frame) is suited for only A2A coverage because of three dips in A2G region for both planes (0° and 90°) as presented in TABLE I. Directivity of the UAV wireless station coverage also increases in all single antenna placement scenarios because of the reflector properties of UAV body frame. Therefore, multiple antenna systems are required to enhance coverage and to get complete UAV wireless station A2A-A2G functionality.

2) Distributed Multi-Antenna System Coverage

Multiple antennas can be placed on the single structure in two different configurations such as collocated and distributed configuration. Collocated antenna system are used as an array when high directional beams are required. On the other hand, distributed antenna system is usually implemented in systems where enhanced coverage is required.

The V-shaped mechanical bases were introduced to provide stable and symmetric structure for mounting of patch antennas without disturbing the UAV flight. The V-shaped mechanical bases, as shown in Fig. 14, consists of an isosceles

right triangle with two and three outer faces which provide tilt to the antenna beam and orthogonal polarization antenna placement. The material of V-shaped mechanical base for antenna placement simulations was selected as PEC to simulate the worst case scenario for coverage.

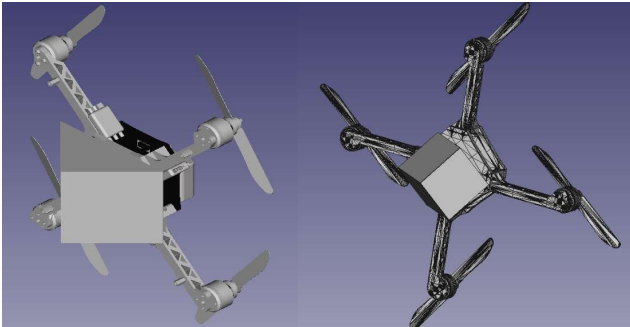


Fig. 14. V-shaped mechanical base attached to the UAV body frame

The implementation of distributed multi-antenna system (DMS) on UAV wireless station consists of mounting orthogonally polarized patch antennas on stable platform in a limited area. The patch antennas are placed in the centre of the outer slit of V-shaped mechanical base in order to maintain the symmetry of resultant UAV wireless station coverage. **Two patch antenna based DMS placement** scenarios as shown in Fig. 15, in such a way that top figure has 1) *both patch antenna ports directed towards air*, bottom right figure has 2) *both patch antennas ports directed towards ground* and bottom left figure has 3) *one antenna port directed towards air and second antenna port towards ground*.

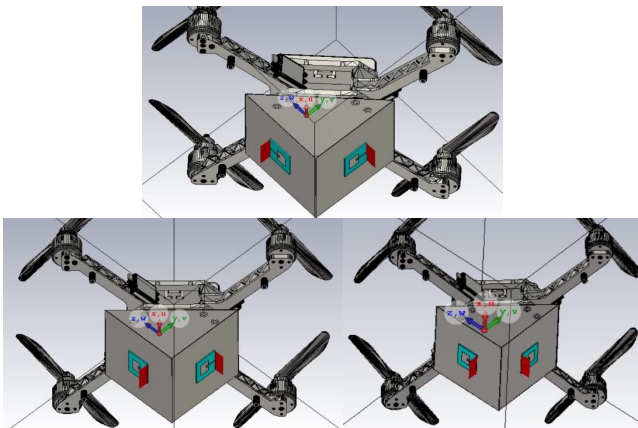


Fig. 15. Two patch antenna based DMS placement scenarios

The comparison of UAV wireless station coverage for defined two patch antenna DMS configurations at cut plane 0° is shown in Fig. 16, and at cut plane 90° is shown in Fig. 17.

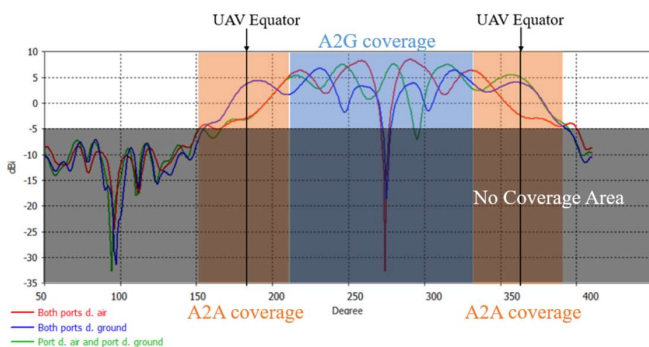


Fig. 16. Radiation pattern of integrated two patch antenna based DMS configurations and UAV body frame for cut plane 0°

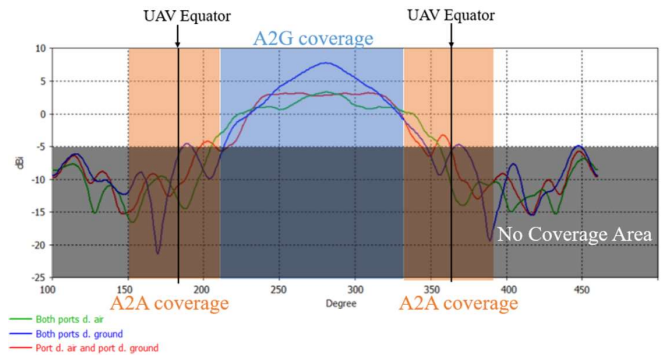


Fig. 17. Radiation pattern of integrated two patch antenna based DMS configurations and UAV body frame for cut plane 90°

The A2G and A2A angular spread comparison of UAV wireless station coverage for all two patch DMS placement scenarios at cut plane 0° and 90° using defined figure of merits is presented in TABLE II.

TABLE II: 2 PATCH ANTENNA DMS PLACEMENT COVERAGE COMPARISON

2 Patch Antenna Based DMS	A2G Coverage		A2A Coverage	
	Cut Plane 0°	Cut Plane 90°	Cut Plane 0°	Cut Plane 90°
Both antenna ports directed towards air	210° to 330° with one null at 271° (5° wide)	210° to 330°	150° to 210° and 330° to 390°	No coverage along equator
One antenna port towards air and other towards ground	210° to 330° with one null at 295° (3° wide)	210° to 330°	150° to 210° and 330° to 390°	No coverage along equator
Both antenna ports towards ground	210° to 330° with one null at 275° (5° wide)	210° to 330°	150° to 210° and 330° to 390°	No coverage along equator

The coverage results comparison of all two patch antenna DMS configurations at both cut planes 0° and 90° show that all scenarios provide A2G coverage for both planes but with the presence of one dip/null (width defined in table) which create no coverage area for ground users. Moreover, all scenarios provide A2A coverage in only one plane. Therefore, different **three patch antenna based DMS placement** scenarios were considered to get 3D coverage as shown in Fig. 18, in such a way that left figure has 1) *all patch antenna ports directed towards ground* and right figure has 2) *all patch antennas ports directed towards air* with respect to flying UAV wireless station position. The antenna placements in both configurations are also orthogonally polarized.

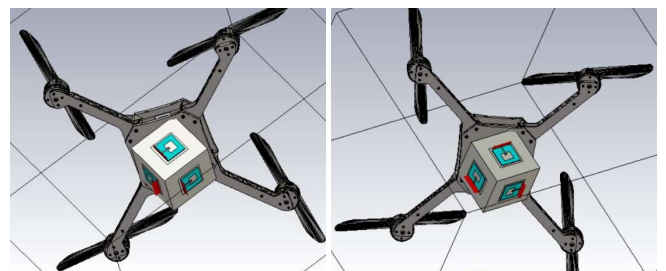


Fig. 18. Three patch antenna based DMS placement scenarios

The UAV wireless station coverage comparison for defined three patch antenna DMS configurations at cut plane 0° and 90° are shown in Fig. 19, and Fig. 20, respectively.

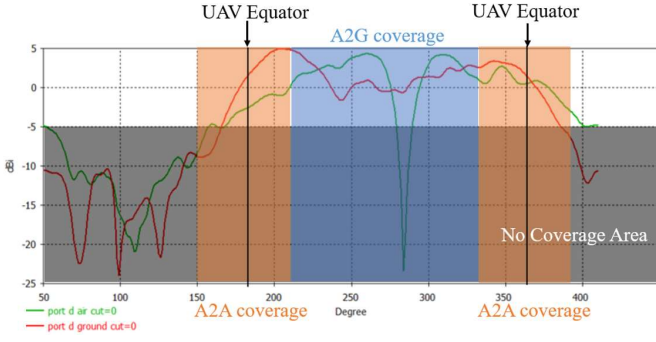


Fig. 19. Radiation pattern of integrated three patch antenna based DMS configurations and UAV body frame for cut plane 0°

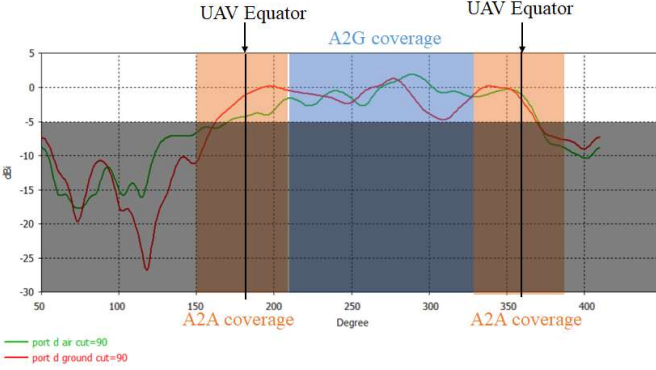


Fig. 20. Radiation pattern of integrated three patch antenna based DMS configurations and UAV body frame for cut plane 90°

The comparison of UAV wireless station coverage for all three patch based DMS placement scenarios at cut plane 0° and 90° using defined figure of merits is presented in TABLE III.

TABLE III: 3 PATCH ANTENNA PLACEMENT DMS COVERAGE COMPARISON

3 Patch Antenna Based DMS	A2G coverage		A2A coverage	
	Cut Plane 0°	Cut Plane 90°	Cut Plane 0°	Cut Plane 90°
All antenna ports directed towards air	210° to 330° with a null at 283°(10° wide)	210° to 330°	157° to 210° and 330° to 390°	170° to 210° and 330° to 370°
All antenna ports directed towards ground	210° to 330°	210° to 330°	165° to 210° and 330° to 386°	161° to 210° and 330° to 369°

The comparison of UAV wireless station A2G-A2A coverage for all antenna placement scenarios show that single antenna placement only helps to achieve either A2G or A2A coverage, however, two and three patch antenna based DMS scenarios allow to enhance the coverage with the introduction of single nulls/dips which results in the no-coverage zones within A2G coverage. Within DMS scenarios, only *three patch antenna based DMS placement scenario with all antenna ports directed towards ground* has 3D UAV wireless coverage for A2G-A2A coverage without nulls though it also doesn't covers all the A2A region but perform well around equator. Moreover, the directivity of the DMS configurations for multi-antenna placement has also reduced which results in the enhancement of UAV wireless station coverage.

As coverage is key indicator of UAV wireless station TRS figures, the integrated antenna system on UAV body frame using *three patch antenna based DMS placement scenario*

with all antenna ports directed towards ground can be used for performance evaluation of UAV wireless station A2G or A2A connectivity.

IV. INFLUENCE OF PROPELLER ROTATION ON UAV WIRELESS STATION TRS FIGURES

A. Key Metrics Characterizing TRS Figures Subject to Influence of Rotating Propellers

The UAV wireless station A2A connectivity will be directly influenced by the scattering and backscattering from its own rotating propellers and rotating propellers of other UAV wireless stations. The *micro-Doppler effect* is the key indicating metrics for the influence due to the backscattering of rotating propeller on UAV wireless station TRS figures. The micro-doppler effect is the introduction of sidebands due to the variation in rotating propeller RCS.

The RCS is the measure of scattering from object/target, therefore, a quasi-static RCS study was used to simulate the RCS of the propeller in order to estimate the influence of rotating propeller on backscattered wave.

RCS also known as electromagnetic signature of object/target tells us about how much energy is reflected back to the source after striking the object/target which is also important for the detection of object. RCS usually depends on multiple factors; operating frequency (transmitter), material of target, geometry of target, incident angle and reflected angle of EM wave. The RCS ' σ ' is given by:

$$\sigma = \lim_{r \rightarrow \infty} 4\pi r^2 \frac{|E^s|^2}{|E^i|^2} \quad (2)$$

Where E^s is the scattered electric field intensity while E^i is the incident electric field intensity. ' r ' is the distance between the source and target.

The rotating propeller influence on the UAV wireless station TRS figures workflow is shown in Fig. 21.

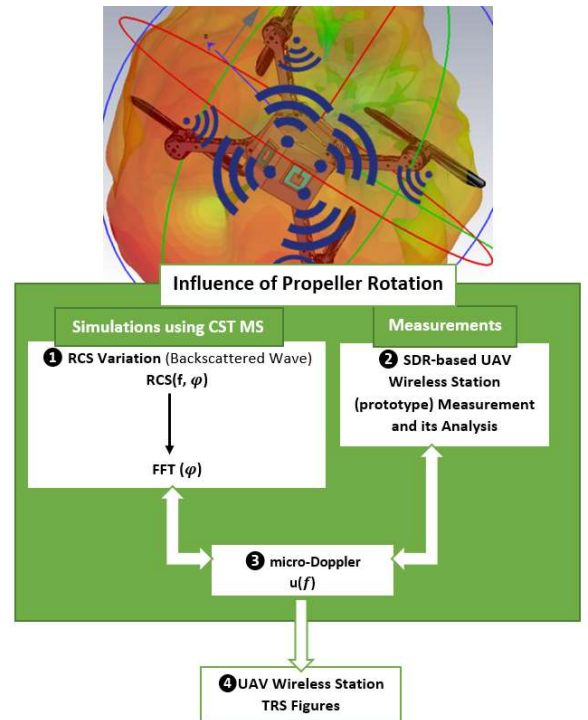


Fig. 21. Influence of UAV propeller rotation on TRS figures work flow

The RCS variation of UAV propeller was computed in first step with respect to frequency and rotating angle as scattering depends on both factors. Next step is to take a fast fourier transform of variation in RCS of rotating propeller to get influence on TRS figures in terms of periodic harmonics as known as micro-Doppler signature. SDR-based UAV wireless station (prototype) measurements and its analysis also produces the micro-doppler signature (key indicator of TRS figures).

B. Simulation Methodology of RCS of Rotating Propellers

The RCS simulations can be done in CST microwave studio by defining a plane wave source on one boundary box wall. The illumination of an object/target by using a plane wave source depicts the far field scenario where electromagnetic waves radiated from an antenna in far field region. The RCS simulation can be done at any particular angle by placing the object/target at the required orientation with respect to plane wave source [32]. After defining the plane wave source and boundary box, the next step is to import designed propeller 3D model and set the material of propeller model to PEC in order to resemble the scattering from lossy conductors.

Finite Integration Technique (FIT), Finite Element Method (FEM) and Moment of Method (MOM) CST microwave studio EM solvers can be used to simulate static object RCS from which FEM and MOM EM solvers are usually preferred for single frequency simulations. The 1D discretization of MOM EM solver works better for one dimensional wire like structures for example propellers whereas the FEM EM solver is suitable for complex 3D structures which in the end effects the output. Performance of all these solvers were also compared by conducting RCS simulations on propeller. Moreover, FEM takes more computational load as compared to MOM solver [33]. Therefore, MOM solver was used to study the influence of propeller rotation on UAV wireless station TRS figures.

The change in propeller RCS was studied at different frequencies and rotation angles for different propeller orientation. The rotating propeller modulates the backscattered wave depending on the incident angle of EM wave and axis of rotation ' Ω ' of propeller. For this purpose, quasistatic rotating propeller can be considered for RCS simulations because the rotational frequency is very small compared to the excitation frequency ($\Omega \ll \omega$). Rotating propeller simulations were conducted at different rotating angles to create the quasi-static rotating propeller, keeping the angle of plane wave and UAV wireless station frequency constant.

C. Numerical Investigations

The orientation of propeller (length 38.15cm) is defined by an angle theta ' θ ' between incident EM wave direction (along Y-axis, $\mathbf{k} = -k\hat{\mathbf{y}}$) and axis of rotation ' Ω ' of the propeller as shown in Fig. 22. Two major orientations of propeller are when 1) the angle between incident EM wave and axis of rotation is zero ($\theta = 0^\circ$ or propeller rotation plane is normal to incident EM wave) and 2) $\theta = 90^\circ$ (propeller rotation plane is parallel to incident EM wave). *Propeller rotation plane normal to incident EM wave orientation ($\theta = 0^\circ$) depicts the illumination of UAV wireless station own propellers with respect to its antenna placement for A2A scenario whereas propeller rotation plane parallel to incident EM wave orientation ($\theta = 90^\circ$) represents the illumination of propellers*

of neighbouring aerial nodes. The orientation of propeller is not perfectly normal when EM incident wave illuminates its own UAV propellers but it is close to normal, therefore, $\theta \approx 0^\circ$ is considered to see the influence of propeller rotation on broadside of propeller.

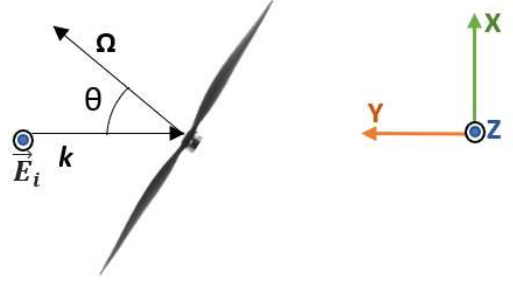


Fig. 22. Orientation of Propeller with respect to Incident EM Wave.

The RCS simulation scenarios for two major orientations of propeller with respect to incident EM wave ($\theta = 0^\circ$ & 90°) and rotation angles ' φ ' are described here one by one. The Fig. 23 represents the RCS simulation scenario when propeller rotation plane is normal to EM incidence orientation ($\theta = 0^\circ$) where ' φ ' is the rotation angle with respect to H-plane, which means propeller length is along H-plane when propeller rotation angle is $\varphi = 0^\circ$ and along E-plane when $\varphi = 90^\circ$.

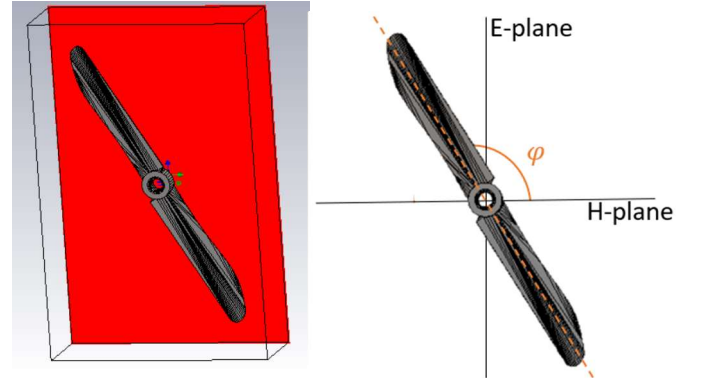


Fig. 23. Propeller RCS simulation scenario in CST Microwave Studio ($\theta = 0^\circ$ normal incidence and φ is 120°)

The next RCS simulation scenario is for propeller rotation plane parallel to EM incidence orientation ($\theta = 90^\circ$) in order to see the influence of propeller rotation from the side of propeller as shown in Fig. 24.

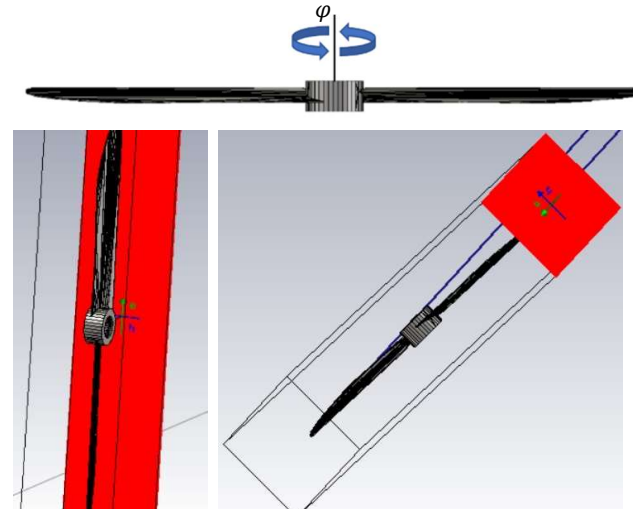


Fig. 24. Propeller RCS simulation scenario ($\theta = 90^\circ$ parallel incidence)
(a) Propeller complete side visible (b) Propeller blade tip visible to EM wave

In this scenario, the propeller rotation is along E or H-plane all the time. The ‘ φ ’ shows the angle of rotation where $\varphi = 0^\circ$ when complete side of propeller is visible to the plane waves and $\varphi = 90^\circ$ when only tip of blade is visible to the plane waves.

1) Analysis of Propeller RCS Simulations for Different Frequencies

This section discusses the variation in RCS with respect to change in frequency in order to see the impact of backscattering along E and H-plane in $\theta = 0^\circ$ orientation and along E or H-plane in $\theta = 90^\circ$ orientation.

The series of RCS simulations were conducted when propeller rotation plane is normal to EM wave direction ($\theta = 0^\circ$) at different frequencies and at propeller rotation angles $\varphi = 0^\circ, 15^\circ, 30^\circ, 90^\circ$ and 105° as shown in Fig. 25. The instantaneous propeller rotation angles were used to see the impact of propeller orientation with respect to EM wave’s E and H-plane as CST microwave studio doesn’t allow to simulate multiple angles at a same time.

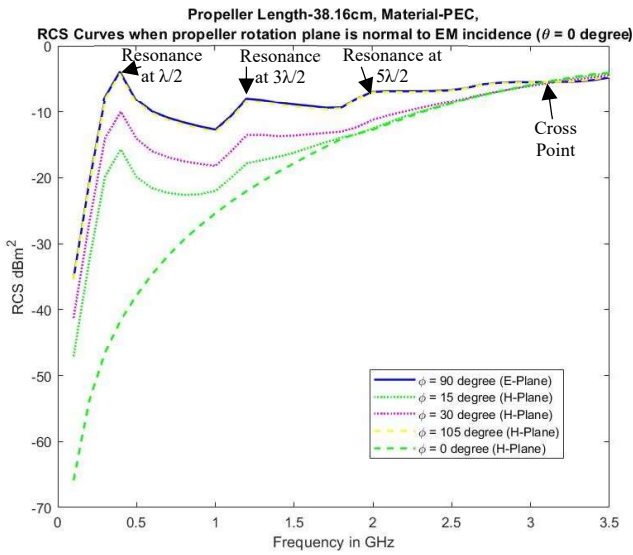


Fig. 25. RCS vs Frequency curves for propeller orientations $\theta = 0^\circ$ and rotation angles $\varphi = 0^\circ, 15^\circ, 30^\circ, 90^\circ, 150^\circ$.

The results (RCS curves at different rotation angles) represent the scattering behaviour of propeller with the change of frequencies. The RCS curve for $\varphi = 90^\circ$ (propeller length along E-plane) is maximum whereas it is minimum for $\varphi = 0^\circ$ (propeller length along H-plane) when compared with $\varphi = 15^\circ, 30^\circ$ and 105° propeller rotation angles. The value of RCS increases with frequency for all RCS curves. The RCS curves for $\varphi = 90^\circ$ and $\varphi = 0^\circ$ crosses each other at 3.1 GHz (-5.46 dBm^2). Within all rotation angles, the maximum RCS value is -3.91 dBm^2 at first resonance point 0.4 GHz for $\varphi = 90^\circ$ which shows the maximum scattering from the propeller. The resonance points/peaks are also visible in RCS curves when electric field component of incident EM wave is present along the propeller’s length. The resonant frequency of propeller is given by $(l \approx \lambda/2)$ where ‘ l ’ is the physical length of propeller which is equal to 393.18 MHz for our propeller ($l = 38.15 \text{ cm}$). The resonance points are spotted in the curves at almost 400 MHz, 1.2 GHz and 2 GHz where the propeller’s electrical length is equal to $\lambda/2, 3\lambda/2$ and $5\lambda/2$ (first three odd multiples of $\lambda/2$), respectively. These resonance points/peaks are present because odd multiples of half wavelength dipole antennas have maximum of its current distribution in the middle of

antenna (feed point) and antenna transmits/receives most of the radiation at the area where current is maximum.

Another important observation is that the RCS curves oscillates between the maximum RCS curve ($\varphi = 90^\circ$) and minimum RCS curve ($\varphi = 0^\circ$) when propeller rotation is normal to EM wave direction ($\theta = 0^\circ$) which will be further investigated for more rotation angles in the next Section.

The next RCS simulation scenario is for propeller orientation when propeller rotation plane remains parallel to EM incidence ($\theta = 90^\circ$) at rotation angles ($\varphi = 0^\circ$ and $\varphi = 90^\circ$) and along EM wave’s E and H-plane, separately. In this rotation plane, the propeller will be along one specific EM wave plane (E or H-plane) for all rotation angles. The RCS curves for the above described propeller orientations when side of propeller is illuminated by EM waves are shown in Fig. 26.

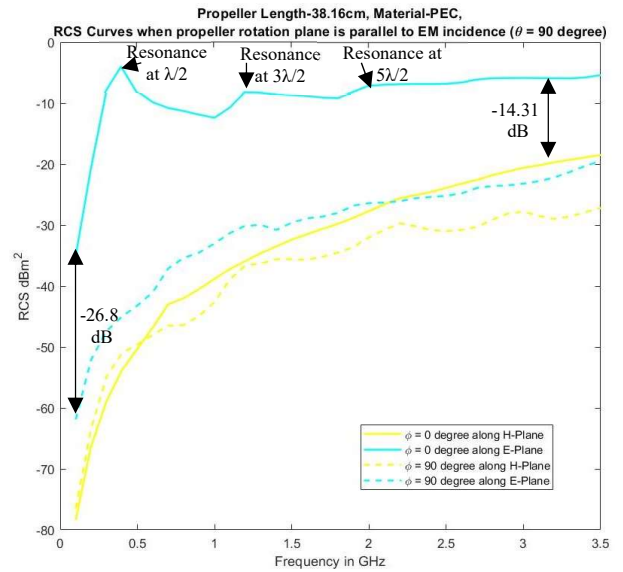


Fig. 26. RCS vs Frequency curves at propeller orientations $\theta = 90^\circ$ and rotation angles $\varphi = 0^\circ, 90^\circ$ along H-plane and along E-plane.

The RCS results for rotation angle $\varphi = 0^\circ$ and $\theta = 90^\circ$ orientation (blue and yellow solid lines) show that the curve along E-plane follows the same pattern as that of RCS curve for $\theta = 0^\circ$ orientation when electric field component of incident EM wave is present along the propeller’s length. The resonance points are also visible at propeller physical length ($\lambda/2, 3\lambda/2$ and $5\lambda/2$). On the other hand, the RCS curve along H-plane shifted -14.31 dBm^2 at 3.1 GHz below as compared to the normal incidence propeller ($\theta = 0^\circ$) RCS curve along H-plane due to reduced surface area of propeller interacting to EM waves. The downward shifting of this RCS curve also shifts the cross point between RCS curves ($\theta = 90^\circ, \varphi = 0^\circ$) along E and H-planes. However, the RCS curves for same propeller orientation ($\theta = 90^\circ$) but for rotation angle $\varphi = 90^\circ$ in E and H planes are represented by blue and yellow dashed lines, respectively. In this scenario, the RCS curve along E-plane plane wave also shifted downwards by 26.8 dBm^2 (at 100MHz) and resonance points also vanish as compared to same propeller orientation ($\theta = 90^\circ$) and E-plane curve at $\varphi = 0^\circ$ due to minimum exposed area (propeller blade tip). The H-plane curve maintains its level but also lost its smoothness as compared to H-plane at $\varphi = 0^\circ$.

The RCS variation with frequency at different propeller orientations shows the variation of RCS with the increase of

frequency for propeller orientation along E-plane and H-plane. The series of CST microwave studio simulations of propeller orientations ($\theta = 0^\circ$ & 90°) at different frequencies are shown in Appendix B. In next section, the propeller RCS is measured at different rotating angles at fixed frequency in order to estimate the influence of RCS variation of rotating propeller on UAV wireless station TRS figures.

2) Analysis of Propeller RCS Simulations for Different Rotation Angles

The variation in rotating propeller RCS with time is further investigated by using the quasi-static approach (different static time) at 2.4GHz and 3.3GHz keeping the plane waves orientation fixed. The rotating propeller can be modelled as quasi-static rotating propeller when the rotational frequency of propeller is very small compared to the excitation frequency of wireless station ($\Omega \ll \omega$). Quasi-static rotating propeller modelling also helps to simulate it in CST microwave studio for 10° steps of angle variation for each simulation. The backscattered field from the rotating propeller is considered in order to see its influence on UAV wireless station TRS figures. The change in RCS with time along different propeller rotation angle is important to study, how rotating propeller impacts the UAV wireless station TRS figures.

The backscattered field produced from the rotating propeller depends on the induced current due to incident electric field. The induced current can be calculated by considering the incident electric field component which is along the length of the propeller also known as radial component of electric field [33]. The radial component of electric field can be written in corotating coordinates as

$$E_{rad}(r, t) = E_z^i \sin(\Omega t) e^{j\omega t} e^{-jkr \sin(\theta) \cos(\Omega t)} \quad (3)$$

Where E_z^i is the incident electric field magnitude of EM wave propagating towards Y-axis (electric field component is along Z-axis) and $\varphi = \Omega t$ is the angle of rotation of the propeller. The term $e^{-jkr \sin(\theta) \cos(\Omega t)}$ represents the phase delay in the incident EM wave.

The radial component of electric field can be expressed as an infinite series of harmonic functions by expanding phase delay term for $\theta > 0^\circ$ as mth-order bessel function of first kind whereas radial component of electric field has only $\sin^2(\varphi)$ (three frequencies components) for $\theta = 0^\circ$ because phase delay term just vanished.

The CST microwave studio simulations were conducted for propeller rotation plane normal to EM incidence ($\theta = 0^\circ$) orientation as shown in Fig. 23. In this propeller orientation, the rotating propeller will be completely along H-plane at $\varphi = 0^\circ$ and completely along E-plane at $\varphi = 90^\circ$. The backscattered wave has the RCS maximum value for all simulations. The RCS_{max} values were plotted against rotation angles at 2.4 GHz and 3.3 GHz for propeller rotation normal to EM incidence ($\theta = 0^\circ$) orientation as shown in Fig. 27.

The RCS vs rotation angle plot at 2.4 GHz represents the $\sin^2(\varphi)$ curve also known as amplitude modulation factor which also verifies the mathematical modelling of rotating propeller in $\theta = 0^\circ$ orientation. The inverted RCS 3.3GHz curve is due to the reason that $RCS_{E-plane}$ and $RCS_{H-plane}$ crosses each other at 3.1GHz and differences between both curves decreases at normal incidence as shown in Fig. 25. The results show that the RCS variation with angle/time (rotating propeller changes rotation angle with time) induces the

amplitude modulation on the backscattered wave due to $\sin^2(\varphi)$ RCS variation.

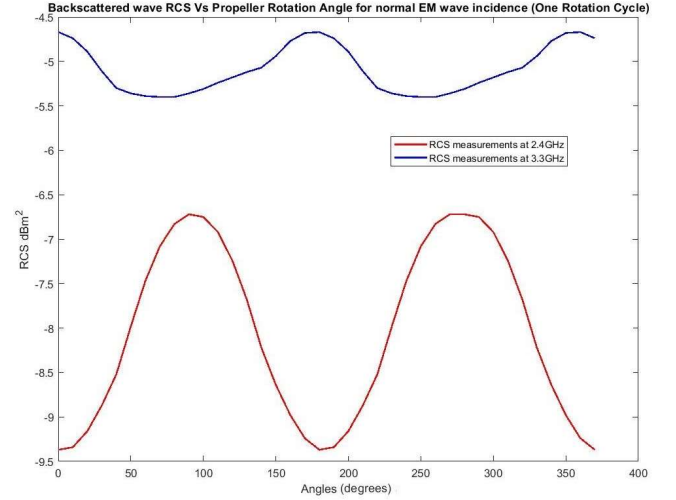


Fig. 27. Backscattered wave RCS_{max} Vs Rotation Angles of a rotating propeller in quasi-static state at 2.4GHz and 3.3GHz (normal incidence)

The $\sin^2(\varphi)$ term in the radial component of electric field at $\theta = 0^\circ$ has influence of rotating propeller in term of three frequency components in frequency domain. The spread of the frequency depends on the rotation speed (Ω) of propellers. The single sided spectrum by taking fast fourier transform of RCS Vs rotation angle curve at 2.4GHz (normal incidence) is shown in Fig. 28. which verifies the influence of rotating propeller in frequency domain on TRS figures.

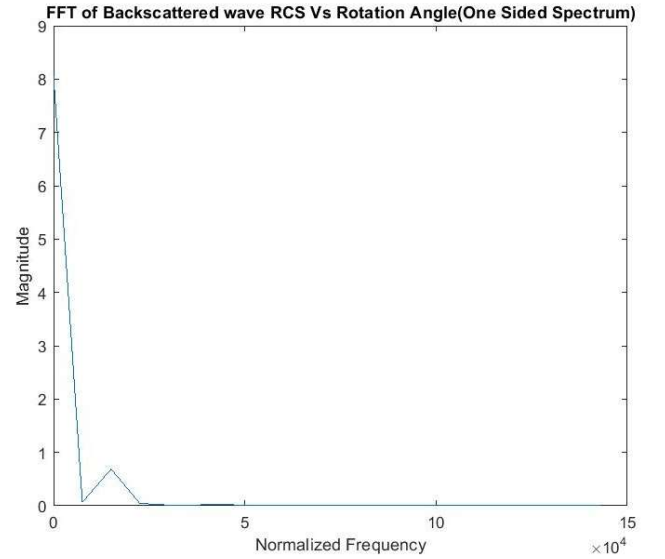


Fig. 28. FFT of backscattered wave RCS_{max} Vs Rotation Angles curve at 2.4GHz (normal incidence)

Similarly, the backscatter RCS simulations were also conducted for propeller rotation plane parallel to EM incidence ($\theta = 90^\circ$) in 10° angle variation steps for one complete rotation (0° to 360°) as shown in Fig. 24. The orientation of EM wave doesn't change with the rotation of propeller in this scenario that's why propeller is set to rotate along E-plane. The tabulated RCS values were later plotted for 2.4 GHz and 3.3 GHz (propeller rotation plane parallel to EM incidence and along E-plane orientation) as shown in Fig. 29.

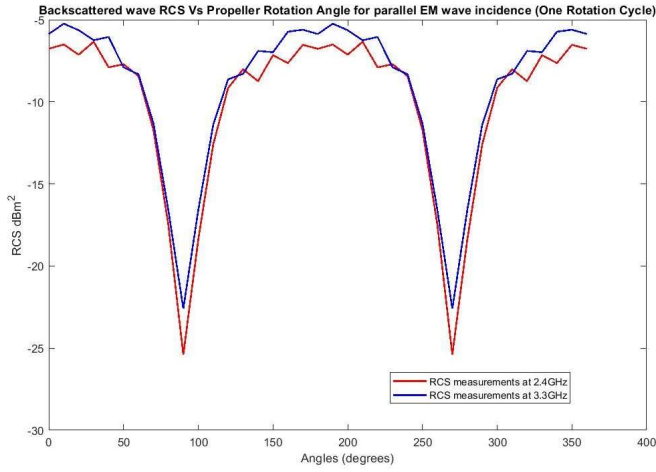


Fig. 29. Backscattered wave RCS_{max} Vs Rotation Angles of a rotating propeller in quasi-static state at 2.4GHz and 3.3GHz (parallel incidence)

The results show that the RCS variation with angle/time (rotating propeller changes rotation angle with time) induces the phase modulation on the backscattered wave which results in infinite series of harmonic functions by expanding phase delay term in frequency domain for $\theta = 90^\circ$. The 2.4 GHz and 3.3GHz RCS curve verifies the propeller rotation induced infinite series of harmonic functions according to Eq.(3) as it has extra frequency components as compared to $\theta = 0^\circ$ rotating plane because of phase delay term also known as phase modulation factor.

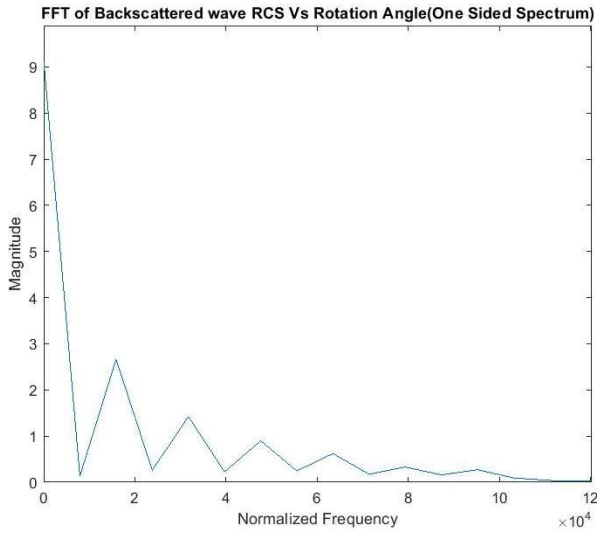


Fig. 30. FFT of backscattered wave RCS_{max} Vs Rotation Angles curve at 2.4GHz (parallel incidence)

The single sided spectrum by taking fast fourier transform of RCS Vs rotation angle curve at 2.4GHz (parallel incidence) is shown in Fig. 30. The periodic harmonics depends on the rotation frequency of propeller. This induced modulation (only three frequency components for $\theta = 0^\circ$ and periodic harmonics for $\theta = 90^\circ$ in frequency domain) is reflected in the TRS figures of UAV wireless station and can be verified by the micro-Doppler measurements of UAV. Micro-Doppler shows the impact of rotating propeller (frequency domain) in terms of periodic harmonics.

The series of CST microwave studio simulations in pictorial form of rotating propeller at orientations ($\theta = 0^\circ$ & 90°) are shown in Appendix B.

V. SDR-BASED PROTOTYPE OF UAV WIRELESS STATION AND MEASUREMENT ANALYSIS

The measurements were planned using the SDR-based prototype of UAV wireless station to study the impact of UAV rotating propellers in terms of induced modulation/periodic harmonics by implementing the Continuous Wave (CW) radar on Nuand BladeRFx40 SDR, discussed in detail in Appendix A.1.

1) SDR-Based UAV Wireless Station (Prototype) Setup

The SDR-based UAV wireless station (prototype) measurement setup consists of a DJI Matrice 100 professional drone (UAV), Nuand bladeRF x40 Software-Defined Radio, Tx/Rx 2.4 GHz whip antennas (a flexible straight wire and has omni-directional radiation pattern), data acquisition using GNU Radio framework, HBM Digital Tachometer and QGroundControl flight control.

The default controller of UAV(DJI Matrice 100) also operates on the ISM band (2.4GHz) which causes a lot of interferences during initial measurements. Therefore, the UAV operating frequency had been shifted to 433 MHz using the R/C (Radio-Controller). The 2.4 GHz (ISM band) was used as an operating frequency for the measurements due to unavailability of license to transmit at 3.3 GHz as European laws require license in order to transmit outside the ISM bands. The R/C controller was used to operate UAV by sending commands via QgroundControl flight control software. The flight control software (QgroundControl) sets propeller rotor speed by sending Pulse Width Modulation (PWM) commands to the UAV.

The SDR-based UAV wireless station (prototype) measurements were conducted in a drone testing hall located at Saxion, Enschede. The testing hall had the dimensions of 17ft \times 17ft. The DJI Matrice 100 UAV strapped to the table is shown in Fig. 31.



Fig. 31. DJI Matrice 100 UAV strapped to the table for safety purpose.

The propellers of DJI matrice 100 UAV are made up of carbon fiber reinforced plastic (CFRP). Each propeller has the length of 13 inches or 33 cm which is close to the length used in the RCS simulations. For safety purposes, the UAV was tied to the table to avoid unexpected take off and stable measurements.

2) Measurement Scenarios

Two measurement scenarios were considered to study the micro-Doppler effect using SDR.

In the first scenario, the off-loaded SDR was placed at a 0.7m and 2.5m distance from the UAV side in order to illuminate the UAV equatorial region using EM waves. This

scenario depicts the SDR interaction to the side of propeller with minimum area of propeller exposed to SDR. The measurements were conducted by placing the UAV at a distance within radiating near field and far field regions. The binary data was acquired using the GNU Radio framework for further processing to analyse the micro-Doppler effect. The first scenario is represented by diagram in Fig. 32.

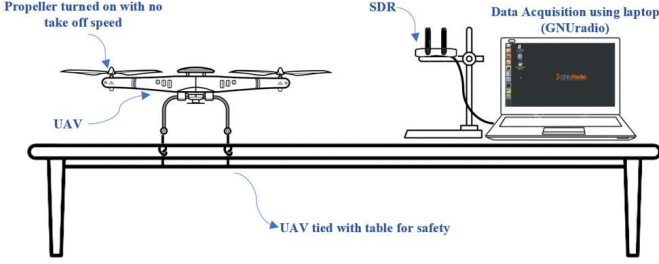


Fig. 32. The off-loaded SDR scenario for measurement

The second scenario was conducted for the loaded SDR orientation (on the UAV) in order to study the direct impact of propellers in different propeller configurations and speeds. In this orientation, the SDR radar Tx/Rx antenna centre is at $\sim 25^\circ$ to 30° angle to the centre of propeller with respect to the rotation plane for propeller 1 & 3. Similarly, SDR Tx/Rx antenna centre is at $\sim 40^\circ$ to 45° angle to the centre of propeller with respect to the rotation plane of propeller 2 & 4. The effect of speed variation between the propellers is also considered during the measurements. The post processing was done using binary acquired data (GNU Radio). The loaded SDR scenario is shown in Fig. 33.

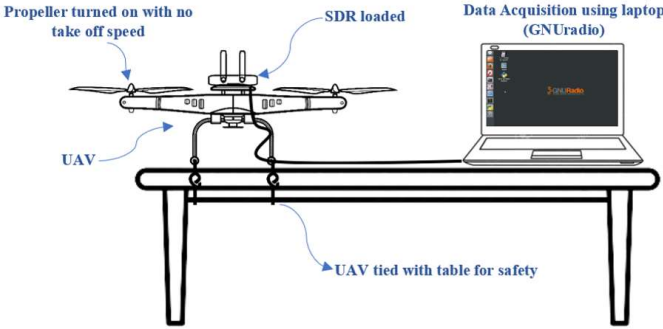


Fig. 33. The loaded SDR scenario for measurement

B. Objectives of Measurement Analysis

The UAV wireless station has two types of motions; translational motion and rotation motion. Doppler signature is caused by translational motion of entire UAV wireless station and on the other hand, micro-Doppler signature due to rotational motion of UAV wireless station own propellers and propellers of secondary aerial nodes in the radio spectrum. The introduction of periodic harmonics due to propeller rotation causes distortion within the UAV wireless station transmission band.

The Short Time Fourier Transform (STFT) can be used to get micro-Doppler signatures from SDR binary data in the form of a time frequency plot. It helps to extract the frequency components from different sections of a time varying signal. The STFT in discrete time can be calculated using the formula:

$$X[n, \omega] = \sum_{m=-\infty}^{\infty} x[m]w[m-n]e^{-j\omega m} \quad (4)$$

Where w is the window and x is the signal.

The Fig. 34 shows the micro-doppler signatures of single propeller rotor (two blades) by applying STFT of small and large window sizes. The picture on the left is the result obtained by applying short window STFT (window length 16) on the binary data while the results when applying the long window STFT (window length 512) is shown in the right picture. The short window STFT gives the modulated waves while the long window STFT produces periodic harmonic lines also known as **HELICOPTER ROTOR MODULATION** due to the induced modulation caused by the rotation of propellers. In HERM lines, the harmonics repeat itself at the multiples of fundamental frequency ' f_0 '. The rotation frequency (Ω) can be calculated using short windowed STFT method where half cycle of the modulated wave is equal to $1/\Omega$ and also from two consecutive harmonic lines in long window STFT which is equal to $N_b\Omega$, where N_b is the number of blades [34].

The blade tip velocity can be calculated by using rotation rate ' Ω ' and length of blade ' L ' as given by:

$$v^{rot} = 2\pi L\Omega \quad (5)$$

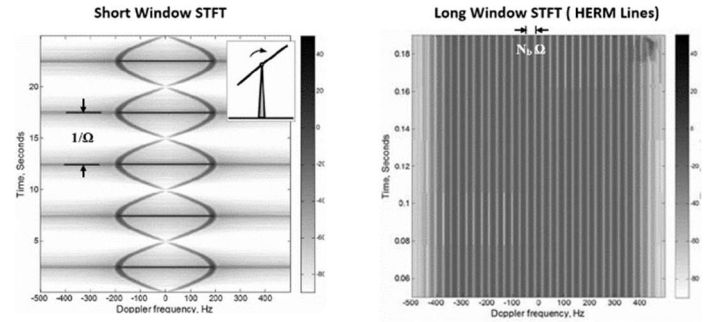


Fig. 34. The micro-Doppler measurements (Time Frequency plot) using short window STFT and long window STFT[34]

C. Measurement Results and Numerical Calculations

The measurements were conducted in order to verify the impact of rotating propeller on UAV wireless station TRS figures in terms of HERM lines and its intensities at different distance scenarios (off-loaded SDR at 0.7 m distance between SDR and UAV, off-loaded SDR at 2.5m distance between SDR and UAV, and loaded SDR).

1) Off-loaded SDR Measurements at 0.7 meter Distance

The measurement setup was created as discussed in the off-loaded measurement scenario for SDR setup at 0.7m distance from UAV. The QgroundControl flight control software was used to select the speed of propellers by selecting proper PWM value. The PWM was set in the range of 1200 to 1300 by keeping in mind the safety of the UAV. At 1400 PWM, the lift was so high that the impact can be seen by upward bending of propellers. Therefore, all the measurements were taken within 1200 to 1300 PWMs range.

The radiating near field measurements can be done by placing SDR setup at the distance of 0.7 m from the UAV as shown in Fig. 35.

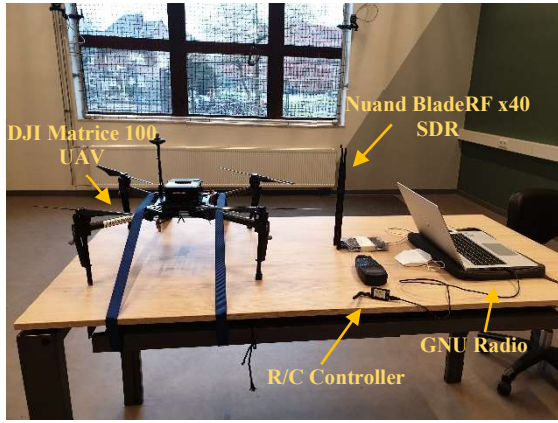


Fig. 35. The radiating near field SDR measurement setup at 0.7m distance

The SDR measurement was started by setting the speed of propellers to 1200 PWM. The value of PWM was then increased in short steps of value 10 at different times till the PWM value of 1300. The acquired data from SDR CW radar was then plotted by taking the long window STFT.

The STFT plot for off-loaded SDR measurements scenario at 0.7 meter distance is shown in Fig. 36. The long window STFT was calculated using the following parameters; Hanning filter of length 512, overlap length of 410 and FFT length of 6144.

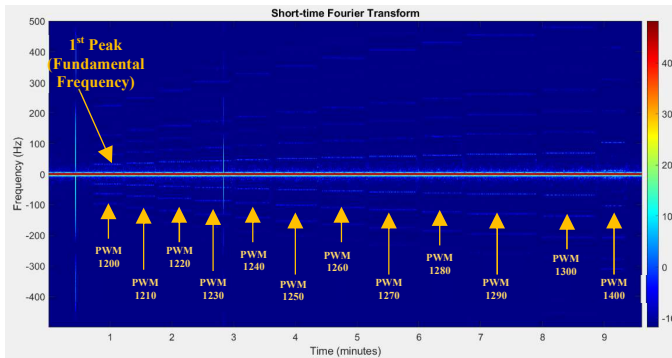


Fig. 36. The long windowed STFT plot of SDR micro-Doppler signature measurement at different rotation speeds.

In STFT plot, the DC line (red line) at zero frequency is recorded by the reflection from the UAV body frame. The 1st peak after the body line is the fundamental frequency ' f_0 ' which is directly proportional to the rotation frequency ' Ω ' which is given by formula:

$$f_0 = N_b \Omega \text{ Hz} \quad (6)$$

where N_b is the number of blades and Ω (rot/s) is the rotation frequency.

The RPM's (Rotation Per Minute) and propeller angular speed ' ω_p ' can be calculated for each fundamental frequency using the formula given below.

$$\text{RPM} \left(\frac{\text{rot}}{\text{min}} \right) = \Omega \left(\frac{\text{rot}}{\text{s}} \right) \times 60 \left(\frac{\text{s}}{\text{min}} \right) \quad (7)$$

The angular frequency can be calculated using the formula:

$$\omega_p = 2\pi\Omega \quad (8)$$

The rotating propeller RPM's can also be estimated using HBM digital tachometer by placing a small strip of reflector on the rotating propeller motor and pointing a digital tachometer laser on it. The RPM's calculated using the

rotating propeller HERM lines were also verified by using the digital tachometer.

The power of first and last (8th) harmonic of the periodic harmonics (HERM lines) induced due to the rotation of propeller at certain angular speed is estimated using STFT plot and presented in TABLE IV along with RPM's estimation using fundamental frequency and tachometer.

TABLE IV: POWER OF 1ST AND LAST HARMONICS FOR OFF-LOADED SDR (0.7 METER) SCENARIO AT VARYING ANGULAR SPEED OF PROPELLER

Fundamental Frequency ' f_0 ' (Hz)	Angular Speed of propeller ω_p (rad/s)	Power of 1st harmonic peak (dB)	Power of last (8th) harmonic peak (dB)	RPM using f_0	Tachometer RPM's
32.46	102	-55.68	-64.41	974	938
35.8	112.5	-55.47	-64.27	1074	1040
39.94	125.5	-54.79	-64.61	1198	1145
43.28	136	-55.7	-62.39	1298	1250
47.42	149	-54.25	-63.64	1422	1348
50.6	158.97	-53.3	-64.42	1518	1459
54.4	170.93	-54.23	-64.15	1632	1567
58.39	183.44	-53.79	-64.00	1752	1660
61.71	193.87	-53.64	-64.34	1851	1760
65.53	205.87	-54.51	-63.98	1966	1870
68.5	215.23	-53.43	-63.12	2055	1960

The measurements analysis of off-loaded SDR at 0.7m scenario helps to observe the impact of side of rotating propeller on UAV wireless station TRS figures when rotation plane is parallel to the EM wave incidence (Fig. 24). The results show the presence of periodic harmonics (HERM lines) within UAV wireless station operating frequency range due to the RCS variation (induced modulation) of rotating propeller. The strength of the harmonic peaks reduce with increasing number of harmonics until it is difficult to separate from the noise floor. STFT plot shows that plot have 8 induced harmonic peaks due to the rotation of propeller at same orientation and for all propeller speeds. The spread of periodic harmonics peaks/components with in the frequency band depends on the rotation speed of UAV propellers. The strength of 1st harmonic peak (≈ -54 dB) and last harmonic peak (≈ -64 dB) lies within the listening range of receiver (-110 dBm or -140 dB) which shows that induced periodic harmonics will be a significant source of distortion for A2A communication link.

2) Off-loaded SDR Measurements at 2.5 meter Distance

The off-loaded SDR measurement was conducted by placing the SDR setup at the distance of 2.5 meter or 100 inch from the UAV within the far field region as shown in the Fig. 37.



Fig. 37. Off-loaded measurement scenario at 2.5m distance

The long window STFT plot for off-loaded SDR-based UAV wireless station (prototype) scenario when UAV is placed at a distance of 2.5 from the SDR setup is shown in Fig. 38.

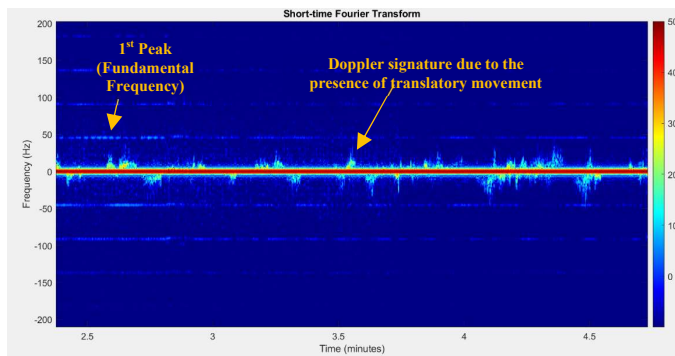


Fig. 38. Long windowed STFT off-loaded SDR scenario at 2.5m

This scenario also depicts the impact of side of rotating propeller on UAV wireless station TRS figures when rotation plane is parallel to the EM wave incidence (Fig. 24) but at the larger distance (2.5 meters) for secondary aerial node case.

The result consists of the HERM lines produced by the induced periodic harmonics (modulation) due to the rotation of propellers at the fixed speed 158.97 rad/s. Multiple doppler shifts along DC line were also present in the results due to translatory movement of object in the measurement area. The periodic harmonics pattern in far field regions also behaves in the similar manner as of near field (off-loaded SDR scenario at 0.7m) which means RCS of propeller behaves in a similar manner for both regions but with different RCS strengths as presented in [26]. HERM method shows that the fundamental frequency of harmonics is proportional to the rotation frequency which can also be used to estimate the UAV/propeller motion dynamics i.e. UAV/propeller speed, UAV/propeller acceleration/deceleration and speed difference between propellers.

3) Loaded SDR Measurements

In loaded SDR scenario as shown in Fig. 39, the SDR is mounted on top of the UAV in order to study the impact of UAV wireless station own propeller's rotation (single or multiple propellers) at steep angles with respect to EM wave. All the propellers lie within the reactive near field (0.4m) range.

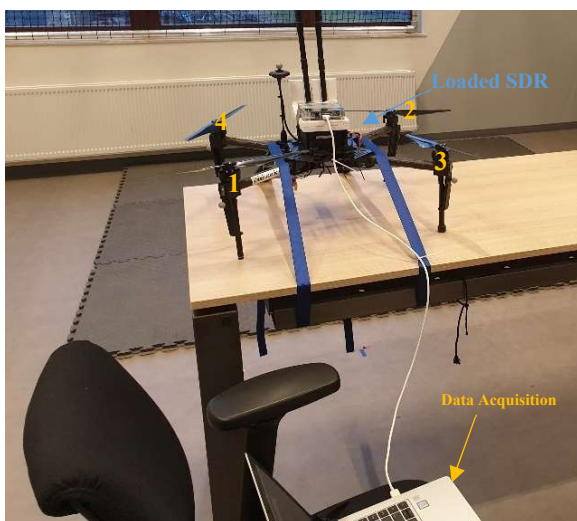


Fig. 39. The loaded SDR measurements setup

As shown in Fig. 40, the SDR is loaded in such a way that SDR TX/RX antennas are facing towards propellers 2 & 4. In this orientation, the SDR will face two propeller's rotation near to the SDR antennas (10 cm) and two propeller's rotation far from SDR antennas (20 cm).

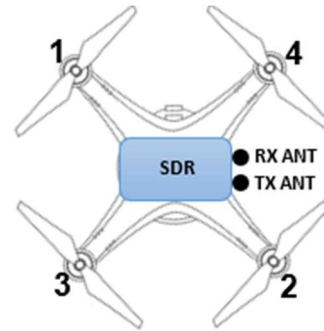


Fig. 40. Loaded SDR placement on the top of UAV

The UAV configuration with respect to SDR placement (Fig. 40) shows that propeller 1 and 2 are diagonal to each other. Similarly, propeller 3 and 4 are also diagonal to each other. All the other combinations are neighbouring propellers (2&4, 1&3, 1&4 and 3&2).

The long window STFT (time vs frequency) plot for only single propeller active at a time for propeller speed (102 rad/s) is shown in Fig. 41. The HERM lines produced due to the rotation of propeller 2 & 4 (near to the SDR TX/RX antennas) have more magnitude as compared to the backscattering due to propeller 1 & 3. The HERM lines are hardly visible due to the rotation of propeller 3 because this propeller is at the farthest distance and propeller is not visible from SDR RX antenna due to SDR height.

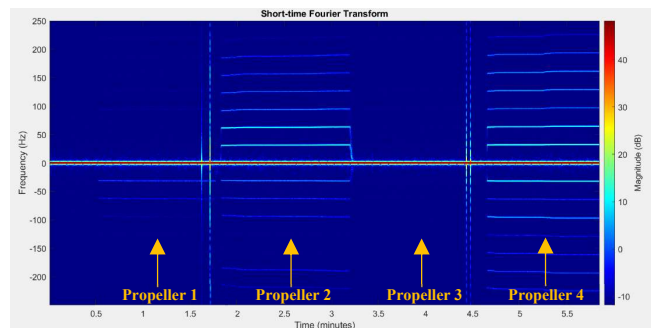


Fig. 41. STFT for loaded SDR scenario with one propeller active at a time

The long window STFT for two diagonal propellers (1&2 and 3&4) active at a time is shown in Fig. 42. The first set of HERM lines are produced due to the rotation of propeller 1 and 2 at a same time. Similarly, the second set of HERM lines are because of propeller 3 and 4 active at a time.

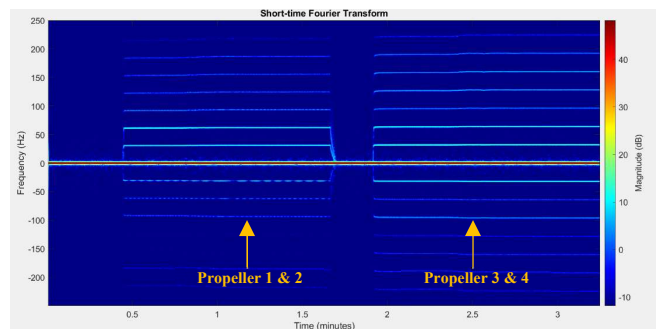


Fig. 42. STFT loaded SDR scenario with two diagonal propellers active

The neighbouring rotating propellers long window STFT plot of all the other combinations (2&4, 1&3, 1&4 and 3&2) are shown in Fig. 43. The HERM lines for propellers 2&4 has two fundamental frequencies which are clearly visible in the higher multiples of harmonics. The propellers 1&3 HERM lines are not significant because these propellers are further away from SDR antennas. The HERM lines for other two combinations are similar and of same strength.

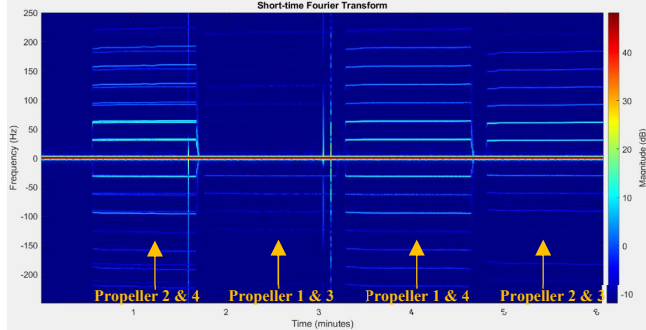


Fig. 43. Long windowed STFT for loaded SDR scenario with two neighbouring UAV propellers active at a time.

The power of the first harmonics for single propeller and dual propeller active at a time measurement for loaded SDR scenario is presented in TABLE V.

TABLE V: POWER OF 1ST HARMONIC PEAK FOR SINGLE PROPELLER AND DUAL PROPELLER ACTIVE AT A TIME FOR LOADED SDR SCENARIO

Angular Speed of propeller ω_p (rad/s)	Power of 1st harmonic peak	Power of 2nd harmonic peak	
		Power of 1st freq. Component	Power of 2nd freq. Component
102 rad/s	-38.12 dB	-43.73 dB	-44.19 dB
158.97 rad/s	-39.77 dB	-43.67 dB	-44.35 dB
215.23 rad/s	-39.15 dB	-43.74 dB	-44.78 dB

The long window STFT plot for all four propellers active in the loaded SDR scenario is shown in the Fig. 44. The two fundamental frequencies can be seen in the plot which was further investigated by measuring difference in rotation speed between propellers using digital tachometer.

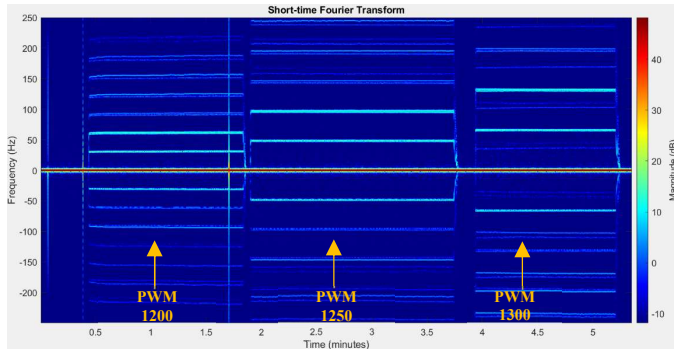


Fig. 44. Long windowed STFT for loaded SDR scenario with all UAV propellers active at a time

The close up of STFT loaded SDR scenario (Fig. 44) shows the presence of two fundamental frequencies which is merged as one in first HERM line whereas it is quite visible from second HERM line as shown in Fig. 45.

The change in the rotation speed between the propeller motors was also verified by collecting the reading of each propeller's rotation speeds using the digital tachometer. The speed of propeller 2 are 908, 1412, and 1920 RPMs while for propeller 4 are 938, 1440, and 1954 RPMs for 1200, 1250 and

1300 PWMs, respectively. These propellers have significant speed difference while other rotates at the same speed. This difference of speeds cause two fundamental frequency components when propeller 2 and propeller 4 are active.

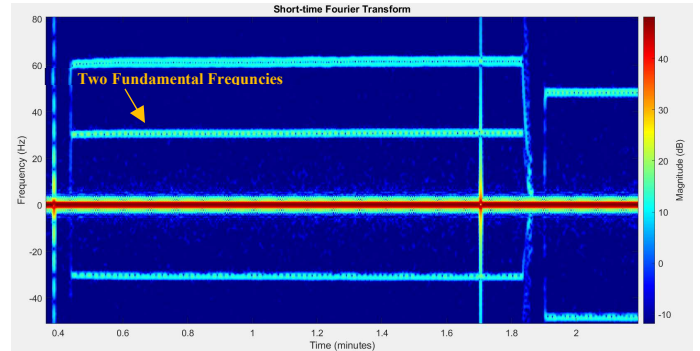


Fig. 45. Close up of STFT loaded SDR scenario having two fundamental frequencies due to difference in propellers speed.

The strengths of HERM lines are measured at three different angular speeds for loaded SDR for all propeller active scenario as presented in TABLE VI.

TABLE VI: POWER OF 1ST AND 2ND HARMONIC PEAK FOR ALL PROPELLER ACTIVE AT A TIME FOR LOADED SDR SCENARIO

No. of Propellers	Power of 1st harmonic peak
1 (Propeller 1)	-63.64 dB (3rd peak) 1 st peak not clearly visible
1 (Propeller 2)	-43.75 dB
1 (Propeller 3)	-63.89 dB (3rd peak) 1 st peak not clearly visible
1 (Propeller 4)	-42.41 dB
2 (Propeller 2&4)	-38.9 dB
2 (Propeller 1&3)	-62.85 dB
2 (Propeller 1&4)	-42.12 dB
2 (Propeller 2&3)	-43.84 dB

The SDR-base UAV wireless station measurements in this scenario helps to observe the impact of all rotating propellers on UAV wireless station TRS figures for $\theta \approx 30^\circ$ (propeller 1&3) and $\approx 45^\circ$ (propeller 2&4). The results show that the presence of periodic harmonics (HERM lines) within UAV wireless station operating band due to the RCS variation at different rotation angles with time. The strength of the harmonic peaks reduce with increasing number of harmonics until it is difficult to separate from the noise floor. STFT plot shows that the strength of 1st harmonic peak (≈ -39 dB) for all propeller rotating which also lies within the listening range of receiver (-110 dBm or -140 dB) whereas two different fundamental frequencies are visible from 2nd harmonic.

The comparison of power of 1st harmonic line/peak at same speed (158.97 rad/s) for all measurement scenarios is presented in TABLE VII.

TABLE VII: COMPARISON BETWEEN POWER OF 1ST HARMONIC PEAK FOR ALL MEASUREMENT SCENARIOS

Scenarios	Power of 1 st harmonic peak at 158.97 rad/s
Off-loaded SDR is at 0.7m from UAV	-53.3 dB
Loaded SDR	-39.77 dB
Off-loaded SDR is at 2.5m from UAV	-56.36 dB

The comparison between the strength of 1st harmonic peak for all measurement scenarios show that the strength is maximum at loaded SDR scenario which means that UAV wireless station experience most significant distortion/degradation of transmission due to its own propeller's rotation. On the other side, strength of HERM lines for off-

loaded SDR scenarios are also significant with respect to the SDR receiver sensitivity (-110 dBm or -140 dB) to disturb the A2A communication. However, the strength of harmonics reduce by increasing the distance from 0.7m to 2.5m which will further reduce when the distance between UAV wireless stations increases up to 100 meters (for UAV sensor networks). Harmonics are visible until 8th harmonic in STFT plot because the remaining harmonics have strength comparable to noise floor that's why indistinguishable. The RCS of the propellers of UAV is very low ($> -5 \text{ dBm}^2$ or 0.316 m^2). Therefore, we can establish that the backscattering from the propellers of secondary UAV wireless station can be reduced to insignificant level in order to distort the A2A communication. However, A2A flying UAV wireless station measurement setup is required to exactly estimate the influence of secondary UAV wireless station propellers at larger distances.

VI. SUMMARY, TAKE-AWAYS AND FUTURE WORK

A. Summary

The characterization of TRS figures were studied for a small rotary wing UAV based wireless station. TRS figures of the UAV wireless station is defined by antenna placement on UAV body frame in order to get the required coverage along with the scattering influence of its rotating propellers. The coverage of the UAV wireless station for A2A-A2G scenarios set the key indicator for UAV wireless station TRS figures. For this purpose, the coverage was explored via CST simulation in the southern sphere of UAV wireless station for ground users and in elevation angles spreading beyond equator towards northern hemisphere for users in air (secondary UAV wireless stations). The position of antenna on UAV body frame is important for symmetric coverage and directivity of coverage also increases because of the influence of UAV body frame. Different two patch and three patch antenna based distributed multi-antenna systems were implemented to improve the UAV wireless station coverage in both A2A-A2G scenarios. The DMS scenarios comparison show that three patch antenna DMS configuration with all antenna ports directed towards ground has improved 3D UAV wireless coverage towards southern hemisphere (210° to 330°) for A2G applications and A2A elevation coverage extended towards northern hemisphere (161° to 210° and 330° to 369°).

Simulations and measurements were also conducted to characterize the scattering influence of UAV wireless station rotating propellers on its TRS figures. For this purpose, *micro-Doppler effect* is the indicator to show scattering influence due to the backscattering of rotating propeller. The RCS simulations show the RCS value of the backscattered wave increases with the increase of frequency. The increase is gradual when the propeller length is completely along the H-plane of the EM waves but the increase is sharp until first resonance point (at $\lambda/2$) then becomes steady, along with peaks at odd multiples of resonance points, for propeller length having component along E-plane. The quasi-static propeller rotation was used to model induced periodic harmonics (modulation) in the backscattering from rotation of propeller. Simulation modelling shows that the backscattering has only amplitude modulation (three frequency components in frequency domain) when propeller rotation plane is normal to EM incidence ($\theta = 0^\circ$) whereas we get the infinite series of harmonics for propeller orientation $\theta > 0^\circ$. The periodic harmonics (depends on rotation frequency), also known as

micro-Doppler effect, was verified by conducting the measurement campaign using SDR-based UAV wireless station (prototype) and DJI Matrice 100 UAV. Measurements were conducted for off-loaded SDR and loaded SDR scenarios in order to analyse the influence of UAV propellers at different distances and propeller orientations. The strength of backscattering from UAV propeller for loaded SDR scenario has the most significant influence on the UAV wireless station transmission. Similarly, the influence of UAV rotating propellers at the $\theta \approx 90^\circ$ (rotating plane is parallel to EM waves) was also measured at the distance of 0.7m and 2.5m. The SDR-based UAV wireless station (prototype) receives the 1st harmonic strength of -53.3 dB at 0.7m and -56.36 dB at 2.5 m for same propeller speed (158.97 rad/s) which also causes distortion of UAV wireless station transmission.

B. Take-Aways

The following takeaways can be deduced from the results;

- To characterize UAV wireless station TRS figures, three patch antenna (orthogonally polarized) based DMS configuration with all antenna ports directed towards ground can be used to get 3D coverage for UAV wireless station A2G-A2A functionality with Naund bladeRFx40 radio.
- The influence of rotating propeller on UAV wireless station TRS figures can be characterized using the quasi-static series of simulations for propeller rotation at different angles of EM wave incidence i.e. RCS variation due to rotating propeller induces amplitude modulation (three frequency components in frequency domain) when EM wave is perpendicular to the rotation of propeller $\theta = 0^\circ$ and phase modulation along with amplitude modulation (infinite series of harmonics) for any arbitrary orientations $\theta > 0^\circ$.
- SDR-based UAV wireless station (prototype) measurements using a UAV target with rotating propellers at off-loaded SDR ($\theta \approx 90^\circ$) and loaded SDR ($\theta \approx 45^\circ$ for two propellers and 30° for other two propellers) scenarios show that the significant strengths of harmonic peaks create distortion within UAV wireless station transmission band.
- SDR measurements equipment can also be used to estimate the UAV motion dynamics using HERM lines from as low as 525 RPM's (or propeller tip velocity 9.07 m/s) to onwards within the percentage error of 4%.

C. Future Work

This research work can be extended in the following dimensions;

- Implementation of cross-polarized dipole antenna system to improve UAV wireless station coverage for A2G-A2A scenarios.
- The SDR radar measurement setup can be used to estimate the motion dynamics/manoeuvring of flying UAV.
- Implementation of background (periodic harmonics) subtraction algorithms to remove rotating propeller influence on UAV wireless station TRS figures.

REFERENCES

- [1] Wikipedia, "Aerial base station" https://en.wikipedia.org/wiki/Aerial_base_station. [last accessed on 16 Dec. 2020].
- [2] E. Vinogradov, H. Sallouha, S. De Bast, M. Mahdi Azari and S. Pollin, "Tutorial on UAVs: A Blue Sky View on Wireless Communication," in *Journal of Mobile Multimedia*, vol. 14 4, pp. 1-74, Nov. 2018.
- [3] B. Vergouw, H. Nagel, G. Bondt and B. Custer, "Drone Technology: Types, Payloads, Applications, Frequency Spectrum Issues and Future Developments," in *B. Custers (ed.), The Future of Drone Use, Information Technology and Law Series*, vol. 27. T.M.C. Asser Press, The Hague, pp. 21-45, 2016, doi:10.1007/978-94-6265-132-6_2.
- [4] H. Wang, H. Zhao, W. Wu, J. Xiong, D. Ma and J. Wei, "Deployment Algorithms of Flying Base Stations: 5G and Beyond With UAVs," in *IEEE Internet of Things Journal*, vol. 6, no. 6, pp. 10009-10027, Dec. 2019, doi: 10.1109/JIOT.2019.2935105.
- [5] J. J. M de Wit, R. I. A. Harmanny and G. Prémel-Cabic, "Micro-Doppler Analysis of Small UAVs," in *2012 9th European Radar Conference*, Amsterdam, pp. 210-213, Nov. 2012.
- [6] C. U. Lee, G. Noh, B. Ahn, J. Won Yu and H. Lim Lee, "Tilted-Beam Switched Array Antenna for UAV Mounted Radar Applications with 360° Coverage," in *Electronics* 2019, 8, 1240, pp. 1-11, Oct. 2019.
- [7] D. Wu, X. Chen, L. Yang, G. Fu, and X. Shi, "Compact and Low-Profile Omnidirectional Circularly Polarized Antenna With Four Coupling Arcs for UAV Applications," in *IEEE Antennas And Wireless Propagation Letters*, vol. 16, pp. 2919-2922, 2017, doi: 10.1109/LAWP.2017.2752358.
- [8] B. R. Motlabane and D. Gray, "TE-monopole radiation pattern DRA for UAVs," in *2012 International Symposium on Antennas and Propagation (ISAP)*, Nagoyo, pp. 499-502.
- [9] Z. Wei and Y. Junfeng, "A Design of Vertical Polarized Conformal Antenna and Its Array Based on UAV Structure," in *International Journal of Antennas and Propagation*, vol. 17, Article ID 9769815, pp. 1-12, Oct. 2017, doi:10.1155/2017/9769815.
- [10] M. S. Sharawi, D. N. Aloï, and O. A. Rawashde, "An embedded uniform linear monopole antenna array in a wing structure of a UAV," *2010 IEEE 11th Annual Wireless and Microwave Technology Conference (WAMICON)*, Melbourne, FL, pp. 1-4, 2010, doi: 10.1109/WAMICON.2010.5461886.
- [11] C. Cheng, P. Hsiao, H. T. Kung and D. Vlah, "Performance Measurement of 802.11a Wireless Links from UAV to Ground Nodes with Various Antenna Orientations," in *Proceedings of 15th International Conference on Computer Communications and Networks*, Arlington, VA, pp. 303-308, 2006. doi: 10.1109/ICCCN.2006.286291.
- [12] P. Héctor Guillermo Parra, M. Víctor Daniel Angulo and G. Elvis Eduardo Gaona, "MEF simulation of radiation pattern of the HyperLOG antenna based on a MicroUnmanned Aerial Vehicle UAV for DVB-T2 signal measurement," pp. 1-5, Jul. 2019.
- [13] F. German, "Ensuring Antenna Performance in Complex Wireless Environment," in *RF AND WIRELESS, ANSYS Advantage*, pp. 21-23, 2017.
- [14] Y. Irfan Mehmood, B. Kiong Lau, B. Bergqvist, "Simulation of internal electromagnetic interference for vehicular antenna performance evaluation," in *2016 10th European Conference on Antennas and Propagation (EuCAP)*, Davos, 2016, pp. 1-4, doi: 10.1109/EuCAP.2016.7481375.
- [15] F. Bocquet, M. Bekowski, A. Moknache, D. Loricchio, "Antennas and Wireless Devices Interferences Simulation within a Vehicle," in *EMC Europe 2016*, pp. 1-39, Jun. 2016.
- [16] C. Tsai, C. Chiang and W. Liao, "Radar cross section measurement of unmanned aerial vehicles," in *2016 IEEE International Workshop on Electromagnetics: Applications and Student Innovation Competition (IWEM)*, Nanjing, 2016, pp. 1-3, doi: 10.1109/iWEM.2016.7504915.
- [17] S. Azarian, J. Pisane and M. Lesturgie, "Experimental RCS acquisition system: Using software defined radio to build a classification dataset," in *2013 International Conference on Radar*, Adelaide, SA, pp. 476-481, Sep. 2013, doi: 10.1109/RADAR.2013.6652035.
- [18] L. R. Danoon and A. K. Brown, "Modeling Methodology for Computing the Radar Cross Section and Doppler Signature of Wind Farms," in *IEEE Transactions on Antennas and Propagation*, vol. 61, no. 10, pp. 5166-5174, Oct. 2013, doi: 10.1109/TAP.2013.2272454.
- [19] M. Geoghegan, M. Nusair, "Effect of Rotating Propellers on Telemetry Signals," in *International Telemetering Conference Proceeding*, pp. 1-10, doi: <http://hdl.handle.net/10150/635258>.
- [20] T. Li, B. Wen, Y. Tian, Z. Li and S. Wang, "Numerical Simulation and Experimental Analysis of Small Drone Rotor Blade Polarimetry Based on RCS and Micro-Doppler Signature," in *IEEE Antennas and Wireless Propagation Letters*, vol. 18, no. 1, pp. 187-191, Jan. 2019, doi: 10.1109/LAWP.2018.2885373.
- [21] T. Peto, K. Marak, S. Bilicz and J. Pavo, "Experimental and Numerical Studies on Scattering from Multiple Propellers of Small UAVs," in *12th European Conference on Antennas and Propagation (EuCAP 2018)*, pp. 1-4, Jan. 2018, doi: 10.1049/cp.2018.1081.
- [22] B. Karlsson, "Modeling Multicopter radar return: A study in discrimination of multicopter UAVs from birds," in *Master's thesis in Applied Physics: Chalmers University of Technology*, 2017, pp.1-55, <https://hdl.handle.net/20.500.12380/252180>.
- [23] V. C. Chen, F. Li, S. - Ho and H. Wechsler, "Analysis of micro-Doppler signatures," in *IEE Proceedings - Radar, Sonar and Navigation*, vol. 150, no. 4, pp. 271-276, Aug. 2003, doi: 10.1049/ip-rsn:20030743.
- [24] V. C. Chen, F. Li, S. Ho and H. Wechsler, "Micro-Doppler effect in radar: phenomenon, model, and simulation study," in *IEEE Transactions on Aerospace and Electronic Systems*, vol. 42, no. 1, pp. 2-21, Jan. 2006, doi: 10.1109/TAES.2006.1603402.
- [25] J. M. Taylor and A. J. Terzuoli, "On the concept of near field radar cross section," in *IEEE Antennas and Propagation Society International Symposium 1997. Digest*, Montreal, Quebec, Canada, 1997, pp. 1172-1175, doi: 10.1109/APS.1997.631766.
- [26] A. Huang, P. Sévigny, B. Balaji and S. Rajan, "Fundamental Frequency Estimation of HERM Lines of Drones," in *2020 IEEE International Radar Conference (RADAR)*, Washington, DC, USA, 2020, pp. 1013-1018, doi: 10.1109/RADAR42522.2020.9114676.
- [27] HEXEL, "Unmanned Aerial Vehicles (UAVs)" <https://www.hexcel.com/Resources/UAV>. [last accessed on 16 Dec. 2020].
- [28] GRABCAD COMMUNITY, "ALPHA" <https://grabcad.com/library/alpha-37>. [last accessed on 08 May. 2020].
- [29] T. Hubing, C. Su, H. Zeng and H. Ke, "Survey of Current Computational Electromagnetics Techniques and Software," in *Technical Report Clemson University*, CVEL-08-011.3, pp.1-56, Jun. 2009.
- [30] R. Ghilduta, "Designing as Automatic Gain Control for the bladeRF," in *GRCon 2018*, pp. 1-29, Jan. 2018.
- [31] T. Zhao, H. Wang, Q. Ma, "The coverage method of unmanned aerial vehicle mounted base station sensor network based on relative distance", in *International Journal of Distributed Sensor Networks*, May 2020. doi:10.1177/1550147720920220.
- [32] A. A. Noor Hafizah, M. Y. Haziq Hazwan, A. R. Nur Emileen, R. A. Raja Syamsul Azmir, O. Kama Azura and S. Asem, "RCS analysis on different targets and bistatic angles using LTE frequency," in *2015 16th International Radar Symposium (IRS)*, Dresden, 2015, pp. 658-663, doi: 10.1109/IRS.2015.7226397.
- [33] K. Marák, T. Pető, S. Bilicz, S. Gyimóthy and J. Pávó, "Electromagnetic Simulation of Rotating Propeller Blades for Radar Detection Purposes," in *IEEE Transactions on Magnetics*, vol. 54, no. 3, pp. 1-4, March 2018, Art no. 7203504, doi: 10.1109/TMAG.2017.2752904.
- [34] P. Klaer, A. Huang, P. Sévigny, S. Rajan, S. Pant, P. Patnaik and B. Balaji, "An Investigation of Rotary Drone HERM Line Spectrum under Manoeuvring Conditions," in *Sensors* 2020, 20, 5940, pp. 1-15, Oct. 2020, doi: 10.3390/s20205940.
- [35] Nuand, "Nuand Product Homepage." <https://www.nuand.com/bladerf-1/>. [last accessed on 16 December 2020].
- [36] D. Valerio, "Open Source Software-Defined Radio: A survey on GNUradio and its applications," in *ftw. Technical Report*, FTW-TR-2008-002, pp. 1-26, Aug. 2008.

APPENDIX-A

This appendix shows the SDR CW radar design to study the influence of revolving propellers on UAV wireless station TRS figures.

Following tools have been used for the development of CW radar for characterization of UAV wireless station TRS figures using measurements.

The software-defined radio is the RF communication systems concept in which the RF signal processing is performed using the components (mixers, modulators/demodulators, filters and amplifiers) are implemented using software that were typically performed using hardware components.

The advantage of SDR is to bring flexibility, reusability and reconfigurability for RF communication by changing parameters like sample rate, bandwidth, frequencies etc.

The bladeRF is a midrange (€480) SDR offered by Nuand LLC company. The bladeRF SDR is capable of full duplex communication using independent Tx/Rx paths in the wide frequency range of 300 MHz to 3.8 GHz. In full duplex communication mode, both signal transmission and reception takes place at the same time with 28 MHz channel bandwidth. The bladeRF supports a sample rate of 40 Msps with Tx/Rx 12 bit wide independent sampling. The USB 3.0 interface is available in order to enable high speed and low latency communication between host computer and bladeRF unit. The onboard Altera Cyclone 4E FPGA consists of logic elements and 18 x 18 multipliers that is dedicated for DSP in order to perform high computation signal processing tasks. The FPGA can be programmed using JTAG interface. On the basis of FPGA logic elements, two variants of bladeRF are available in the market that is bladeRFx40 (40 logic elements) and bladeRFx115 (115 logic elements). The bladeRF is also equipped with wideband LimeMicro LMS6002D RF transceiver to convert the digital baseband signals to the RF signals and vice versa. Two gold plated RF SMA (sub miniature version A) connectors are available for Tx/Rx antenna connectivity. The software support is also available for bladeRF from third party SDR development kits such as Simulink MATLAB and GNU Radio [35].

GNU Radio is the open source software development toolkit that is used for the development of digital signal processing algorithms using a flow graph or coding. GNU Radio software development platform provide large variety of signal processing blocks such as modulators/demodulators, filters, mixers etc that helps to develop different SDR applications. It is compatible with multiple SDR platforms such as Nuand bladeRF, HackRF One, RTL-SDR, LimeSDR and NI USRP to develop different radio communication systems. Beside SDR platforms, GNU Radio can also be used standalone for simulation purposes.

GNU Radio Companion (GRC) is the GNU Radio graphical user interface for the development of SDR application using data flow graph. For high computational performance, all the low level signal processing blocks are written in C/C++ language while they are compiled and run using Python scripts [36].

1) SDR Continuous Wave Radar Design

The purpose of radar development is to measure the micro-Doppler effect to verify the rotation motion of propellers.

In CW radar, transmitter transmits the continuous wave of preferred signal type (Sin or Cosine) all the time and estimate the phase shift from the reflected wave. The block diagram of the implementation of CW radar using bladeRF x40 and GNU Radio is shown in Fig. A.1.

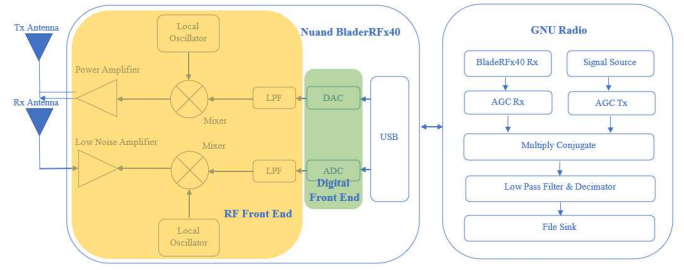


Fig. A.1. Block diagram of CW radar using bladeRFx40 and GNU Radio

The analogue/RF front end of the bladeRFx40 SDR consists of transmission and reception paths that are connected to the Tx/Rx antennas. The transmission path first converts the digital baseband signal into the analogue signal using the DAC which is then passed to the RF front end through the filter in order to limit the baseband signal. The baseband signal is then upconverted to RF signal using the carrier signal by the mixer. The RF signal is then amplified using the power amplifier and transmitted using the transmit antenna. While on the other side, the first component of reception path is low noise amplifier which amplifies the power of the weak strength signal while keeping the same signal to noise ratio. The amplified signal is then down converted by multiplying the signal with the carrier signal. The low pass filter removes the high frequency components from the baseband signal. The RF front end reception path then passes through the analogue baseband signal to the ADC to get the digital baseband signal for further processing. The digital end of SDR comprises of ADC and DAC which converts the digital signal generated using the GNU Radio to analogue for transmission and vice versa for reception.

The GNU Radio software module helps to generate the required signal (Sine wave of 2k frequency) using the *signal source block*. This source signal was transmitted using the *gr-osmocom (osmocom sink) block* which has the carrier frequency of 2.4 GHz. The transmitted signal frequency is given by $f_t = f_0 + f_s = 2.4\text{GHz} + 2\text{KHz} = 2400002\text{KHz}$.

The transmitted signal was generated at sampling rate of 1Msps. The received signal was then collected from SDR using the *gr-osmocom (osmocom source) block*. The reference transmit signal and received signal were passed through the *Automatic Gain Control block* in order to match the amplitude of the carrier signal. Both signals were then passed through the *multiply conjugate block* in order to get the phase shift (Doppler shift) between the signals. The rotational speed produce micro-Doppler shifts at 2.4 GHz signal, therefore the output of multiply conjugate signal should be resampled at lower sample rate. The signal was decimated by 1024 and then filtered. The binary data of resultant signal was then saved using the file sink block for post processing.

APPENDIX-B

This appendix shows the RCS simulation results in pictorial form for following scenarios. The RCS CST simulations for propeller rotation plane normal to EM wave ($\theta = 0^\circ$) orientation and rotation angle at $\varphi = 0^\circ$ (along H-plane) and at $\varphi = 90^\circ$ (along E-plane) for different frequencies are shown in Fig. B.1 and Fig. B.2, respectively. Similarly, RCS CST simulations for $\theta = 0^\circ$ and $\theta = 90^\circ$ orientations for different rotation angles ($\varphi = 0^\circ$ to 360°) are shown in Fig. B.3 and Fig. B.4, respectively.

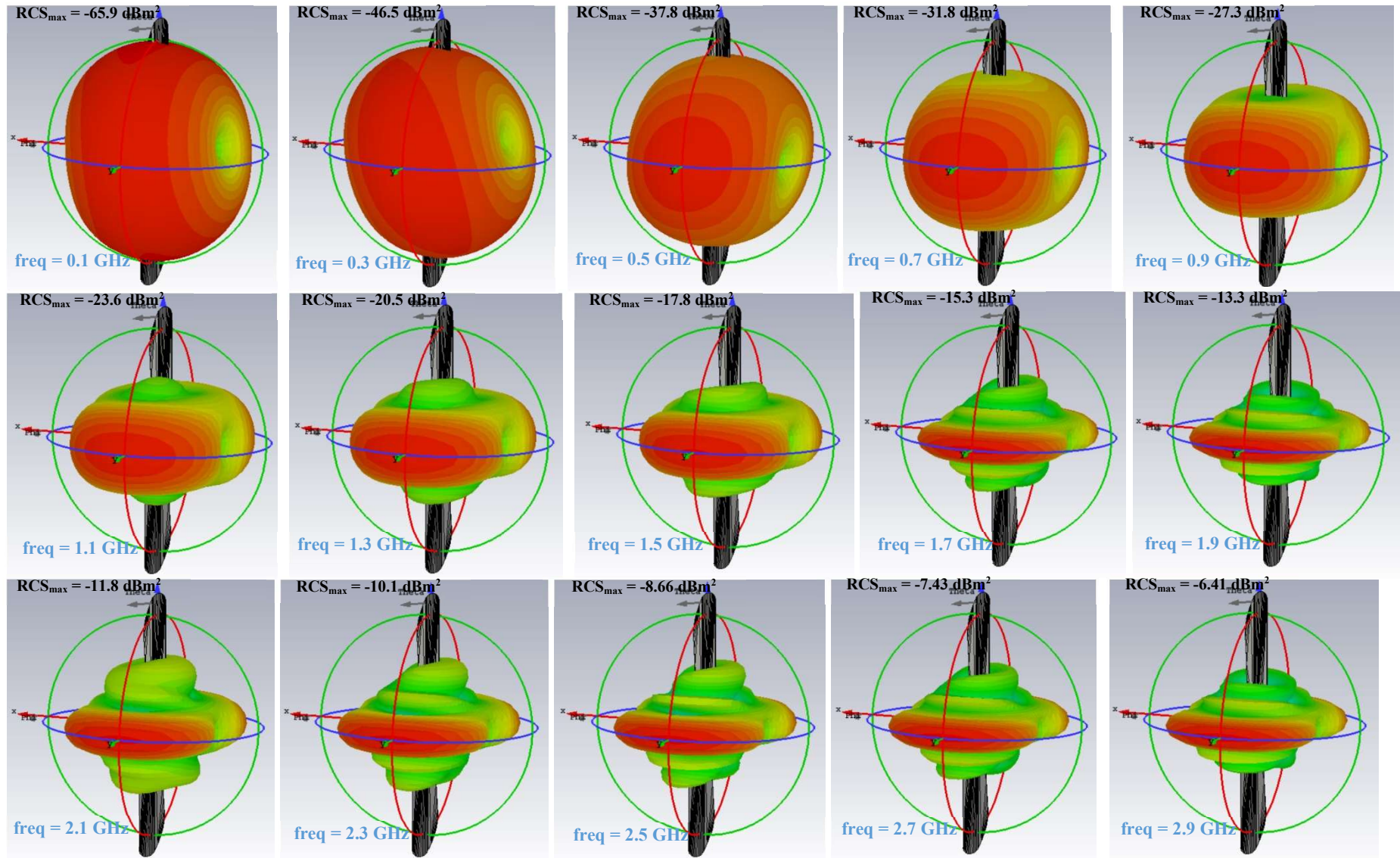


Fig. B.1. Radar Cross Section CST microwave studio simulations for propeller rotation plane normal to EM wave ($\theta = 0^\circ$) orientation for rotation angle $\varphi = 0^\circ$ (along H-plane) at different frequencies

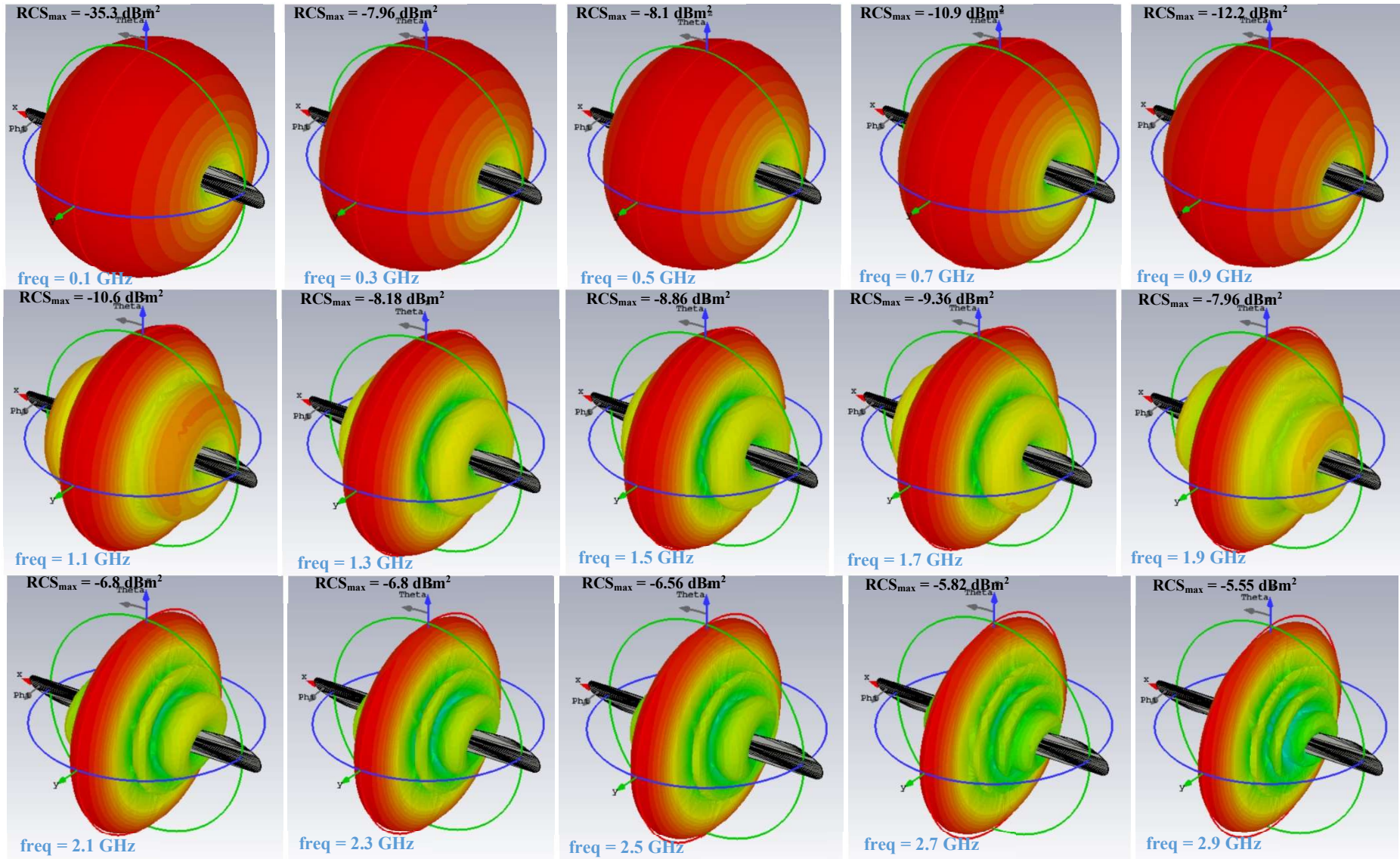


Fig. B.2: Radar Cross Section CST microwave studio simulations for propeller rotation plane normal to EM wave ($\theta = 0^\circ$) orientation for rotation angles $\phi = 90^\circ$ (along E-plane) at different frequencies

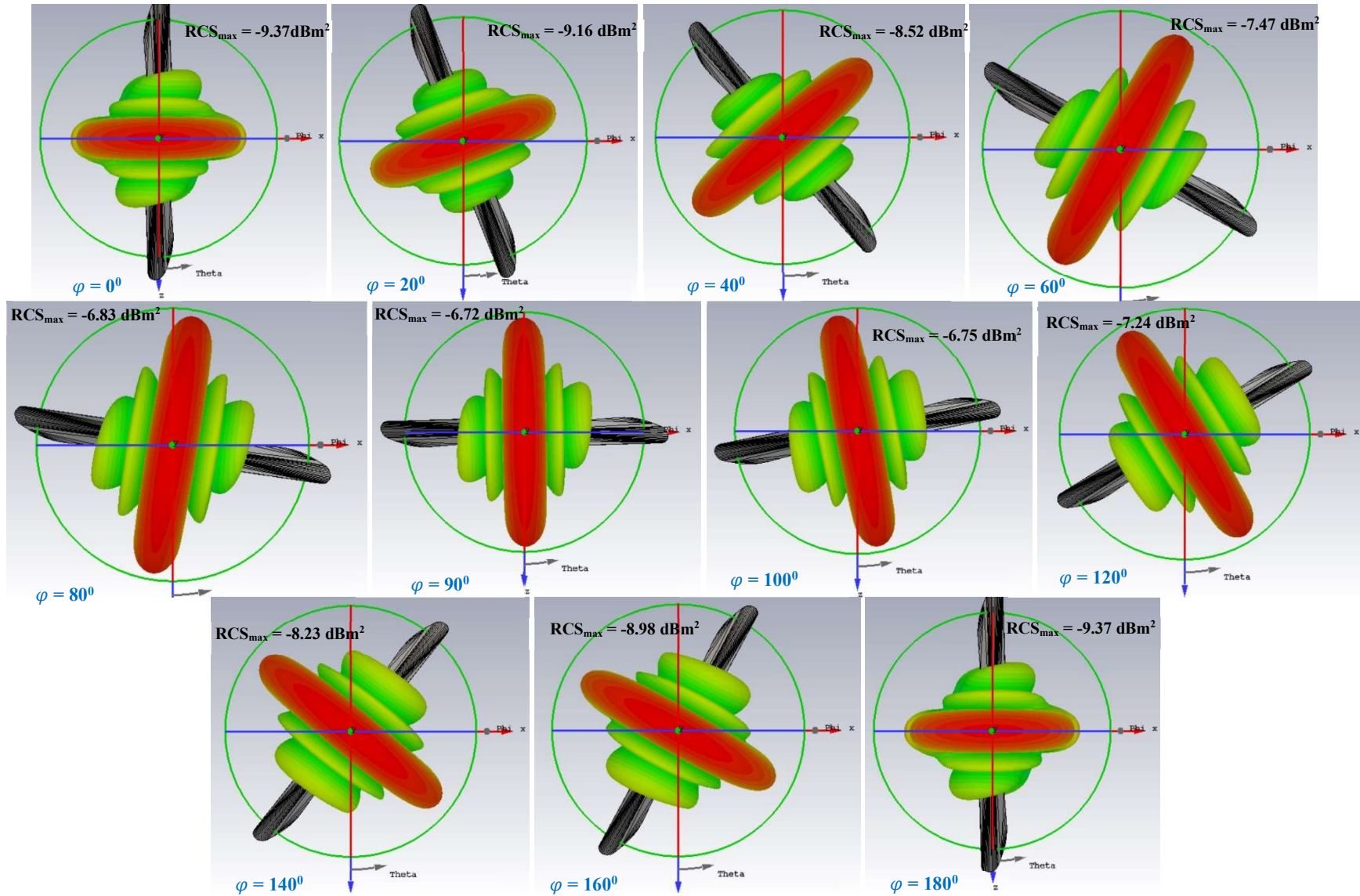


Fig. B.3. Radar Cross Section CST microwave studio simulations for propeller rotation plane normal to EM wave ($\theta = 0^\circ$) orientation at 2.4 GHz and rotation angles $\varphi = 0^\circ$ to 360°

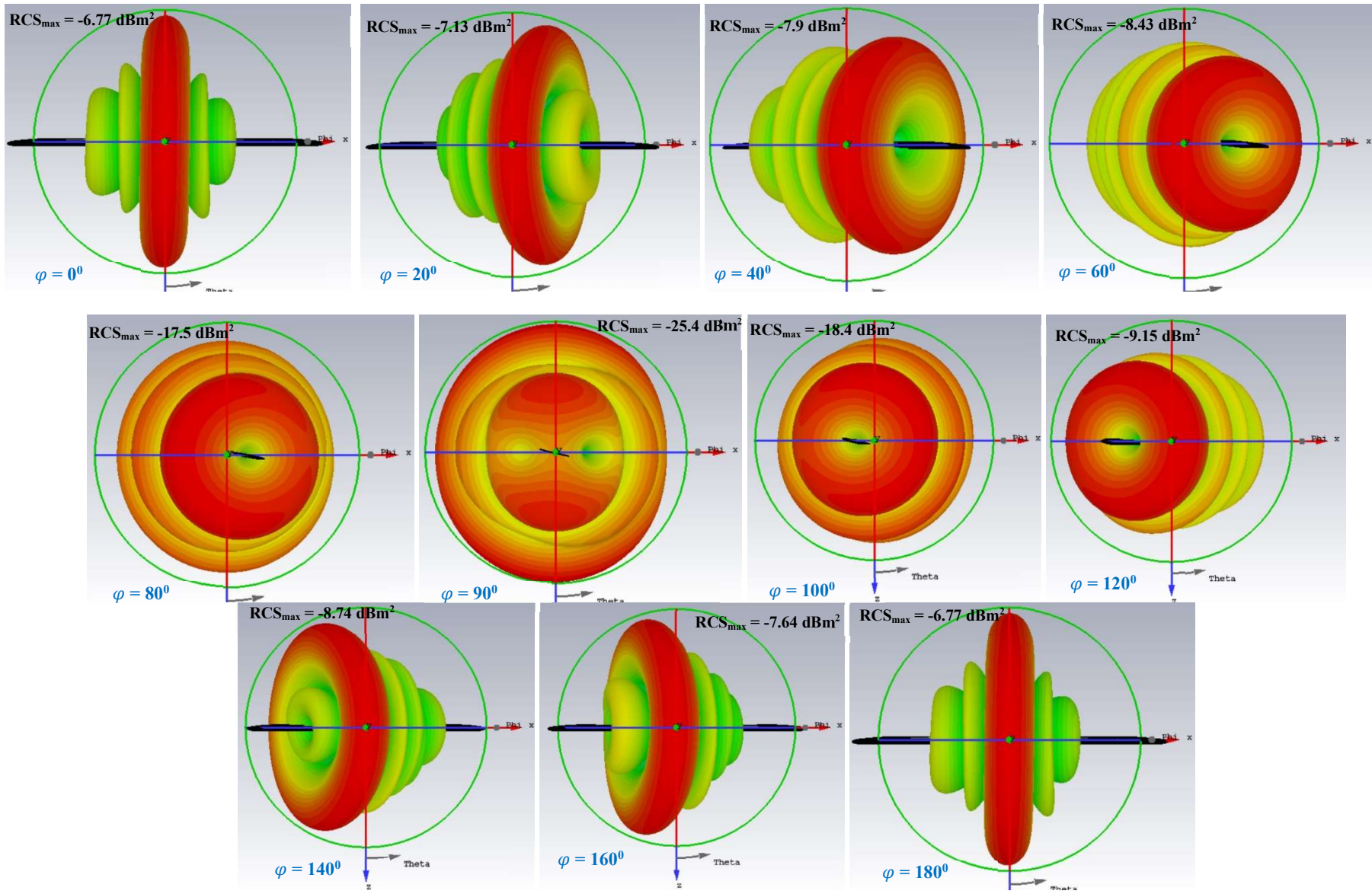


Fig. B.4. Radar Cross Section CST microwave studio simulations for propeller rotation plane parallel to EM wave ($\theta = 0^\circ$) orientation at 2.4 GHz for rotation angles $\varphi = 0^\circ$ to 360°